Neonatal brain injury unravels transcriptional and signaling changes underlying the reactivation of cortical progenitors

Louis Foucault, Timothy Capeliez, Diane Angonin, Celia Lentini, Laurent Bezin, Christophe Heinrich, Carlos Parras, Vanessa Donega, Guillaume Marcy, Olivier Raineteau

Cell Reports

Article

Neonatal brain injury unravels transcriptional and signaling changes underlying the reactivation of cortical progenitors

Graphical abstract

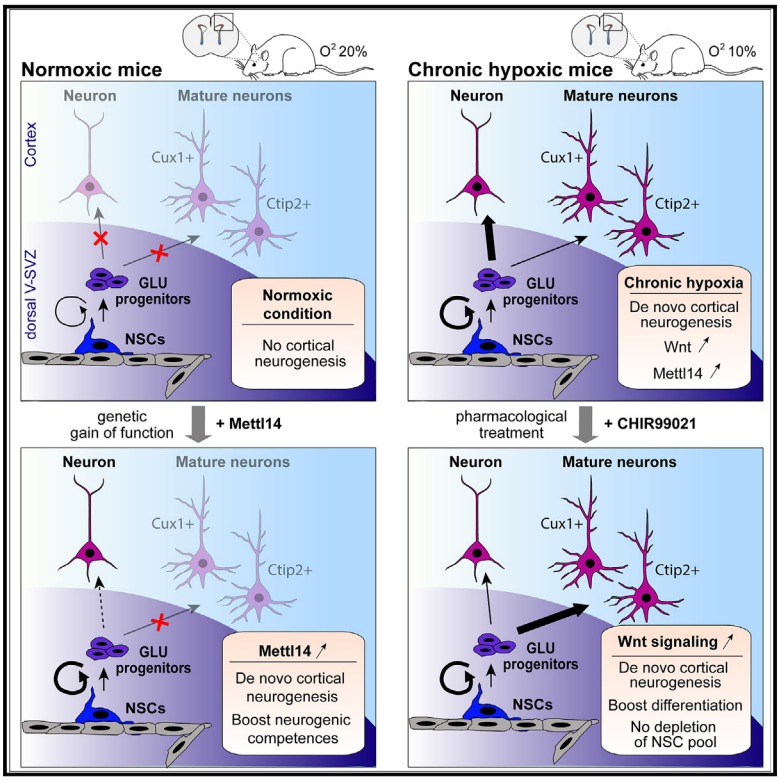

Highlights

- dV-SVZ NSCs reactivate following hypoxia to produce cortical oligodendrocytes and neurons
- Hypoxia reactivates embryonic transcriptional programs in glutamatergic progenitors
- m6a methylation and Wnt/β-catenin activation parallel glutamatergic progenitor reactivation
- Wnt/β-catenin activation does not affect young adult forebrain germinal activity

Authors

Louis Foucault, Timothy Capeliez, Diane Angonin, ..., Vanessa Donega, Guillaume Marcy, Olivier Raineteau

Correspondence

olivier.raineteau@inserm.fr (O.R.), louis.foucault@kuleuven.be (L.F.)

In brief

Foucault et al. point out the reactivation of postnatal NSC embryonic competences within a specific context, such as chronic neonatal hypoxia. They show reactivation of m6a methylation and Wnt/β-catenin within glutamatergic progenitors, which parallels cortical neurogenesis. Moreover, postnatal NSC activation does not lead to germinal activity dysregulation at young adult ages.

Foucault et al., 2024, Cell Reports *43*, 113734
February 27, 2024
https://doi.org/10.1016/j.celrep.2024.113734

CellPress

Cell Reports

CellPress
OPEN ACCESS

Article

Neonatal brain injury unravels transcriptional and signaling changes underlying the reactivation of cortical progenitors

Louis Foucault,[1,*] Timothy Capeliez,[1] Diane Angonin,[1] Celia Lentini,[1] Laurent Bezin,[2] Christophe Heinrich,[1] Carlos Parras,[3] Vanessa Donega,[1,4,6] Guillaume Marcy,[1,5] and Olivier Raineteau[1,7,*]

[1]University Lyon, Université Claude Bernard Lyon1, INSERM, Stem Cell and Brain Research Institute U1208, 69500 Bron, France
[2]University Lyon, Université Claude Bernard Lyon 1, INSERM, Centre de Recherche en Neuroscience de Lyon U1028 - CNRS UMR5292, 69500 Bron, France
[3]Paris Brain Institute, Sorbonne Université, INSERM U1127, CNRS UMR 7225, Hôpital Pitié-Salpêtrière, 75013 Paris, France
[4]Amsterdam Neuroscience, Cellular and Molecular Mechanisms, Amsterdam, the Netherlands
[5]Present address: University Lyon, Université Claude Bernard Lyon 1, Labex CORTEX, Bioinformatics Platform, 69008 Lyon, France
[6]Present address: Amsterdam UMC location Vrije Universiteit Amsterdam, Anatomy & Neurosciences, section Clinical Neuroanatomy and Biobanking, De Boelelaan, Amsterdam 1117, the Netherlands
[7]Lead contact
*Correspondence: olivier.raineteau@inserm.fr (O.R.), louis.foucault@kuleuven.be (L.F.)
https://doi.org/10.1016/j.celrep.2024.113734

SUMMARY

Germinal activity persists throughout life within the ventricular-subventricular zone (V-SVZ) of the postnatal forebrain due to the presence of neural stem cells (NSCs). Accumulating evidence points to a recruitment for these cells following early brain injuries and suggests their amenability to manipulations. We used chronic hypoxia as a rodent model of early brain injury to investigate the reactivation of cortical progenitors at postnatal times. Our results reveal an increased proliferation and production of glutamatergic progenitors within the dorsal V-SVZ. Fate mapping of V-SVZ NSCs demonstrates their contribution to *de novo* cortical neurogenesis. Transcriptional analysis of glutamatergic progenitors shows parallel changes in methyltransferase 14 (Mettl14) and Wnt/β-catenin signaling. In agreement, manipulations through genetic and pharmacological activation of Mettl14 and the Wnt/β-catenin pathway, respectively, induce neurogenesis and promote newly-formed cell maturation. Finally, labeling of young adult NSCs demonstrates that pharmacological NSC activation has no adverse effects on the reservoir of V-SVZ NSCs and on their germinal activity.

INTRODUCTION

During development, neural stem cells (NSCs) generate the cellular diversity of the central nervous system in a strict spatial and temporal manner. NSCs localized within the most dorsal periventricular domain, named the pallium, produce the vast majority of cortical cells, i.e., glutamatergic neurons (corresponding to 80% of cortical neurons) as well as glial cells (oligodendrocytes and astrocytes).[1,2] Cortical cells are produced in sequential waves initiating at embryonic day (E) 12 and extending to the perinatal period.[1,2] Pallial NSCs produce cortical neurons in an inside-out manner, with deep-layer neurons produced first, followed by upper-layer neurons. In mice, it is classically accepted that cortical neurogenesis stops around E17 and that, at this time, NSCs switch their competence to produce glial cells.[3] This neurogenic-to-gliogenic switch, however, only concerns a fraction of NSCs,[4] while others persist within the dorsal subventricular zone.[5,6]

The organization of the postnatal ventricular-subventricular zone (V-SVZ), the main germinal region of the postnatal forebrain, is partly conserved from embryonic development.[7] Its dorsal-most region derives from the embryonic pallium. Besides gamma-aminobutyric acid (GABAergic) progenitors,[6,8] it produces oligodendrocyte precursor cells.[9–11] Moreover, several studies demonstrated the persistence of glutamatergic progenitors within the dorsal domain until early adulthood.[12,13] Remarkably, it was recently suggested that these progenitors are still able to produce sparse cortical glutamatergic neurons during the very first days following birth.[5] However, a rapid downregulation of the Wnt/β-catenin pathway and of posttranscriptional regulator N6-methyladenosine (m6a) signaling parallels a rapid silencing of cortical neurogenesis around birth.[5]

The period of early postnatal development is a period of vulnerability to brain injuries, as well as a period during which spontaneous cellular regeneration has been observed in various injury models.[14–16] Chronic hypoxia is a clinically relevant model of perinatal brain injury. This model recapitulates all physiopathological changes observed in premature, very-low-birth-weight babies.[17] In particular, a loss of cortical volume is observed,[18] accompanied by an enlargement of the ventricles and diffuse

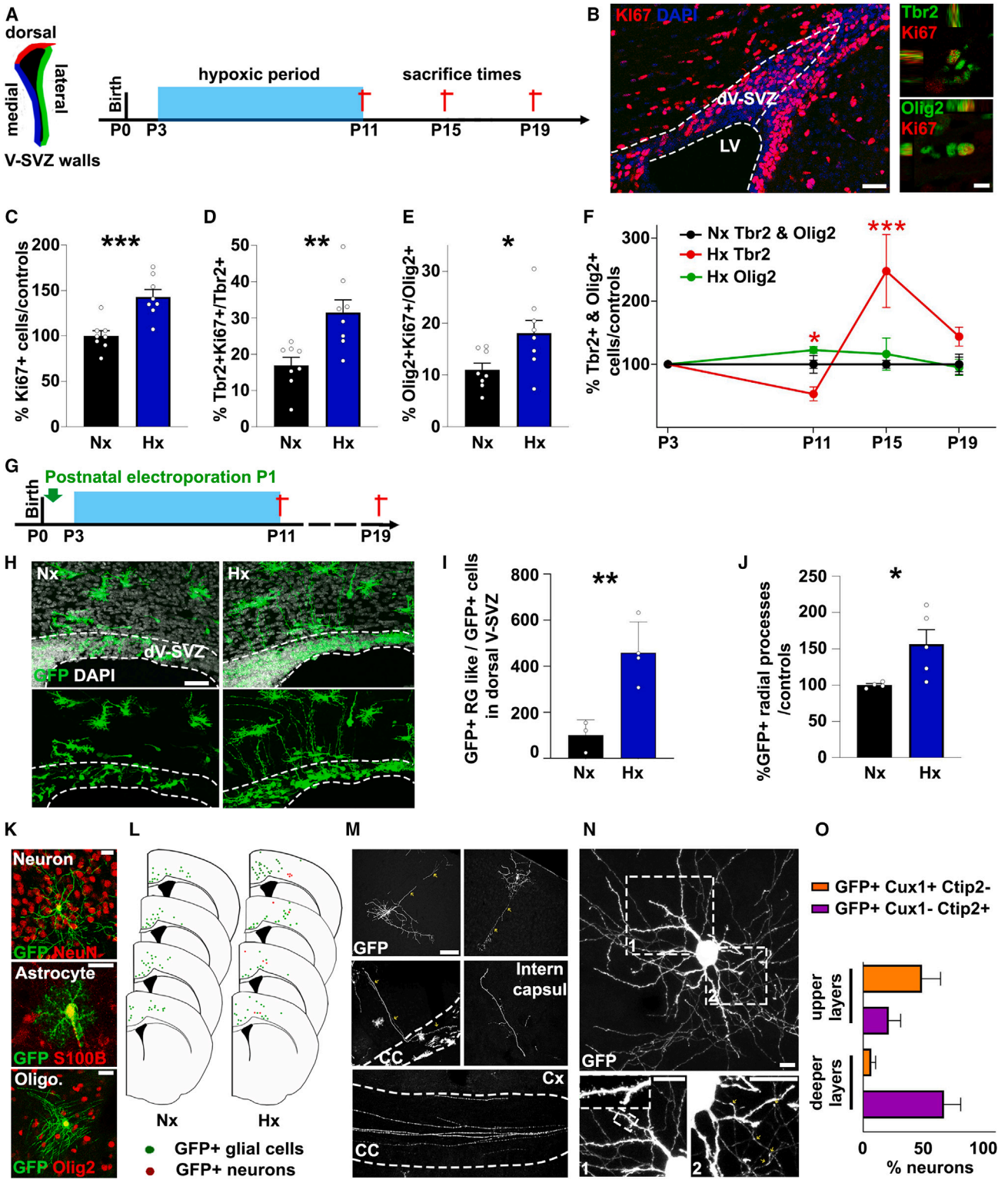

Figure 1. Neonatal chronic hypoxia activates proliferation within the dorsal V-SVZ as well as cellular generation within the cortex

(A) Schematic representation of the V-SVZ domains and experimental procedure. Animals were exposed to chronic hypoxia from P3 to P11 and sacrificed at P11, P15, and P19 for histological analysis.

(legend continued on next page)

white matter injuries.[19] Interestingly, in this model, spontaneous *de novo* cortical neurogenesis and oligodendrogenesis have been described.[17,18,20] Yet, a direct implication of V-SVZ NSCs, and in particular of its dorsal-most domain, in this spontaneous response remains elusive.

Here, we aimed to investigate the response of V-SVZ NSCs to chronic neonatal hypoxia, as well as their competence to produce new cortical neurons and oligodendrocytes. We further aimed at getting insights into the mechanisms underlying their response to hypoxia and to test their amenability to pharmacological manipulation.

RESULTS

Chronic hypoxia disrupts brain maturation and is followed by a spontaneous period of increased germinal activity within the dorsal V-SVZ (dV-SVZ)

We used chronic hypoxia as an established model of neonatal brain injury (Figure S1A).[17] As previously reported, mice exposed to chronic hypoxia showed reduced body and brain weight, paralleled by a significant reduction of cortical volume (Figures S1B–S1D). A closer look at the cortex revealed a doubling of the number of apoptotic cells (i.e., cleaved caspase-3-positive cells) by the end of the hypoxic period (i.e., postnatal day [P] 11), which encompassed cells of both the glial (Olig2+) and neuronal (NeuN+) lineages, including upper- (i.e., Satb2+) and lower-layer (i.e., Ctip2+) cortical projection neurons (Figures S1E and S1F). This was paralleled by marked effects of chronic hypoxia on oligodendrocyte maturation with a reduced expression of the pre-myelinating marker CC1 within oligodendroglial cells (i.e., Olig2+; Figures S1G and S1H), as previously reported,[19] which was paralleled by a reduced intensity of MBP staining (Figures S1I and S1J).

We next analyzed the consequences of chronic hypoxia on the germinal activity of the dV-SVZ over time (Figure 1A). Interestingly, while the size of the dV-SVZ area remained unchanged at the end of the hypoxic period (Figures S1K and S1L), cell proliferation increased within the dV-SVZ (i.e., +43.1% ± 9.7% Ki67+ cells; Figures 1B and 1C), encompassing both glutamatergic (Tbr2+; Figures 1B and 1D) and oligodendroglial (Olig2+; Figures 1B and 1E) progenitors, albeit with different kinetics. Thus, while Olig2+ progenitors were increased by P11 (+22.7% ± 8.3%), Tbr2+ progenitors showed a pronounced reduction at this time point (+53.1% ± 17.6%) but returned to baseline by P19 following a transient blooming at P15 (Figure 1F). This was paralleled by an increase of neuroblasts (DCX+ cells) within the dV-SVZ of mice subjected to hypoxia (Figures S1M and S1N). Together, these results indicate that a neonatal chronic hypoxic period induces a dynamic and lineage-specific response of dV-SVZ germinal activity, which might contribute to the *de novo* cortical neurogenesis observed at later time points.[17–21]

dV-SVZ NSCs and progenitors participate in hypoxia-induced cellular generation

To directly address the contribution of the dV-SVZ to this regenerative attempt, we permanently labeled NSCs and their progeny by electroporation of a CRE plasmid into Rosa-YFP reporter mice or of an integrative (transposon GFP) plasmid in wild-type mice at P1 (Figure 1G). Because the V-SVZ is regionalized (Figure 1A),[7] we performed electroporations restricted to its dorsal- and lateral-most regions (dV-SVZ and lateral V-SVZ [lV-SVZ], respectively; Figure S2A). Interestingly, only fate-mapped cells originating from the dV-SVZ were observed within the cortex at P19 following chronic hypoxia (Figure S2B), while cells originating from the lV-SVZ dispersed within the striatum (Figure S2C). Appearance of fate-mapped cells within the cortex was paralleled by a persistence of GFP+ cells presenting a clear radial glia morphology at the end of the hypoxic period (i.e., P11; Figures 1H–1J). At a later time point (i.e., P19), three different cellular morphologies were clearly distinguishable within the hypoxic cortex, which corresponded to neurons, astrocytes, and oligodendrocytes based on lineage-specific marker expression (NeuN, S100β, and Olig2, respectively; Figure 1K), whereas only glial cells were visualized within the normoxic cortex. GFP+ cells with neuron-like morphology were observed in both upper and deeper cortical layers (Figure 1L). Although they were rare, representing an average estimate of 31 neurons per mouse (among ∼231 GFP+ cells observed within the cortex), some

(B–E) Illustrations (B) and quantifications (C–E) at P11 showing the increase of proliferation within the dV-SVZ (C), in particular of glutamatergic (Tbr2+; D) and oligodendrocyte (Olig2+; E) progenitors, following hypoxia (N ≥ 8). Scale bars: 50 and 10 μm.

(F) Quantifications showing the proportion of glutamatergic (Tbr2+) and oligodendrocyte (Olig2+) progenitors (N ≥ 3) compared to normoxic (Nx) animals at distinct time points following chronic hypoxia.

(G) Schematic representations of experimental procedures. Electroporation was performed at P1 to permanently label NSCs and their progenies, and animals were sacrificed at P11 or P19.

(H–J) Illustrations (H) and quantifications (I and J) illustrating the maintenance of NSCs (i.e., cells presenting a radial morphology, I, and presenting a radial process, J) within the dV-SVZ at the end of the hypoxic (Hx) period (N ≥ 3). Scale bar: 40 μm.

(K) Illustrations of GFP+ cells observed at P19 within the cortex of Hx animals. Neuronal and glial morphologies were clearly distinguishable and correlated with the expression of NeuN, S100β, and Olig2. Scale bars: 20 μm.

(L) Cartography of the type and localization of GFP+ neurons (red dots) and glial cells (green dots) observed within the cortex of representative Nx and Hx mice at P19.

(M) Illustrations of GFP+ neurons within the cortex showing a pyramidal morphology (top left), with a developing axon (top right) going to the corpus callosum (middle left and bottom) and to the internal capsule (middle right). Scale bar: 50 μm.

(N) Illustration of a GFP+ neuron into the cortical area presenting dendritic spines (1) and axonal swellings (2). Scale bars: 10 μm.

(O) Bar plot showing the expression by a fraction of GFP+ neurons of mature layer-specific glutamatergic markers. Note that most Cux1+ neurons are located within superficial cortical layers, while most Ctip2+ neurons are in deeper ones, in agreement with the normal pattern of expression of these markers (n ≥ 9).

*p < 0.05, **p < 0.01, and ***p < 0.001; statistical tests: statistical analysis was performed through parametric unpaired t test for (C)–(E), (I), and (J) and paired t test for (F). Data are presented as mean ± SEM. P0/P3/P11/P15/P19, 0, 3, 11, 15, and 19 days after birth, respectively; dV-SVZ: dorsal ventricular-subventricular zone; LV, lateral ventricle; Nx, normoxic; Hx, hypoxic.

presented a pyramidal morphology (Figure 1M, top left) with axons (Figure 1M, top right) projecting into the corpus callosum (Figure 1M, middle left) toward the contralateral hemisphere (Figure 1M, bottom) and, more rarely, to the internal capsule (Figure 1M, middle right). Further, they frequently showed dendritic spines (Figure 1N, inset 1) as well as branched axons with GFP+ swellings (i.e., putative synaptic sites) along their axons (Figure 1N, inset 2). Interestingly, administration of a thymidine analog (BrdU) at the end of the hypoxic period (P11–P12) led to its colocalization with some GFP+ NeuN+ neurons, demonstrating their production following the hypoxic period (Figure S2E). Moreover, a fraction of the GFP+ neurons expressed mature cortical layer neuronal markers, such as Satb2 and Cux1 for upper layers and Ctip2 and Tbr1 for deeper layers (Figures S2F and S2G), according to their location within upper and deeper cortical layers (Figure 1O). This, together with the observation of a differential morphological complexity of Ctip2+ when compared to Cux1+ neurons (Figures S2H–S2J), suggests appropriate specification of GFP+ newborn cortical neurons following hypoxia.

Together, these results illustrate the reactivation of neuronal competences of the dV-SVZ NSCs following neonatal hypoxia and its participation in *de novo* cortical neurogenesis alongside ongoing gliogenesis.

Transcriptional changes are observed within dV-SVZ progenitors that parallel their reactivation following hypoxia

The observation of both Cux1+ and Ctip2+ hypoxia-induced cortical neurons suggests the reactivation of early transcriptional programs within postnatal glutamatergic (i.e. GLU) progenitors. To investigate these transcriptional changes in more details, we isolated GLU progenitors from the Neurog2$^{CREERT2/tdTomato}$ mice following tamoxifen injection at two embryonic times (i.e., E13 and E15, time of production of deep and upper cortical neurons, respectively), as well as from P12 normoxic (i.e., control) and hypoxic mice, and performed bulk RNA sequencing (Figure S3A). Comparison of normoxic and hypoxic tdTom+ cells at P12 revealed the perturbation of 3,258 transcripts following hypoxia (831 upregulated and 2,427 downregulated, adjusted p value [padj] < 0.01; Figure 2A; Table S1). We first checked if genes associated with gliogenesis (i.e., "positive regulation of gliogenesis" [GO: 0014015] or "regulation of gliogenesis" [GO: 0014013]) were upregulated following hypoxia (i.e., 831 genes). This analysis revealed that only a very restricted number of genes were identified, i.e., Dag1, Bmp4, Kdm4a, and Sirt2, further confirming that hypoxia does not induce ectopic expression of glial genes in Neurog2+ progenitors (Figure S3B). We then focused on genes induced by hypoxia but not enriched at embryonic or postnatal times (i.e., 373 genes; Figure 2B). Interesting, an over-representation analysis (ORA) showed that these genes are involved in RNA processing as well as in the control of cell cycle (Figure S3C), in line with our results showing an increased proliferation following hypoxia (see above). We next focused on genes induced by hypoxia but also showing embryonic enrichment when compared to postnatal time. Indeed, comparison with E13/E15 tdTom+ cells revealed that 42% of the hypoxia-induced transcripts (350/831) showed enrichment in embryonic GLU progenitors, while only 13% (108/831) were enriched in postnatal ones (Figure 2B; Table S1). Since only a small number of these transcripts were specific to the E13 or E15, indicating that hypoxia induces a generic embryonic signature into postnatal progenitors (Figures S3D and S3E), we grouped these two time points in our analysis. Inversely, most transcripts repressed following hypoxia were enriched in postnatal progenitors rather than in embryonic progenitors (21% vs. 7%, respectively; Figure 2B; Table S1). This transcriptional "rejuvenation" was supported by considering the top 50 transcripts enriched in E13/E15 GLU progenitors (based on both p values and fold change [FC]) when compared to postnatal ones. All but 4 of these transcripts were upregulated (FC >2 and p < 10e−6) in GLU progenitors following hypoxia (Figure 2C; see highlighted transcripts; Table S1), a correlation not observed for postnatally enriched transcripts. Further, ORA revealed similarities in Gene Ontology biological process terms related to transcripts enriched in embryonic and postnatal GLU progenitors following hypoxia (top 1,000 transcripts based on padj; Figure 2D; Table S1). Inversely, a similar observation was made when comparing postnatal-enriched and hypoxic-repressed transcripts (Figure S3F; Table S1). Taken together, these results indicate the reactivation of early (i.e., embryonic) transcriptional programs within P12 GLU progenitors following hypoxia, while late (i.e., postnatal) transcriptional changes are globally repressed.

The observation of hypoxia-induced Ctip2+ deep-layer cortical neurons prompts questions about their origin. Indeed, while upper Cux1+ neurons are produced at E15, deep Ctip2+ cortical neurons are produced earlier, at E13. We combined BrdU injections at E13 or E15 and EdU treatment during the hypoxic period to label early- and late-cycling cortical progenitors (BrdU+) and to investigate their contribution to hypoxia-induced cortical neurogenesis (BrdU+/EdU+ neurons) (Figure 2E). Interestingly, BrdU+/EdU+ cortical oligodendrocytes (Olig2+) were observed following both E13 and E15 BrdU injections (Figure 2F), while double-labeled neurons (Cux1+ and Foxp2+ for upper/deeper layers, respectively) were only observed following a BrdU injection at E15 (Figures 2G–2J). To note, BrdU+/EdU+ cortical neurons were observed in upper and deeper cortical layers and expressed corresponding cortical markers, i.e., Cux1 and Foxp2, respectively. Together, these results suggest that hypoxia-induced deep-layer cortical neurons do not arise from the reactivation of a population of early progenitors but rather from a reactivation of embryonic transcriptional programs in late-cycling progenitors.

Transcriptional changes observed within dV-SVZ progenitors following hypoxia converge onto methylation modifications

To gain insight into hypoxia-induced transcriptional changes, we performed an ORA on transcripts induced by hypoxia. We first focused our analysis on the 350 transcripts upregulated by hypoxia and enriched in embryonic cortical progenitors (Figure 3A; Table S2). This analysis highlighted upregulation of transcripts related to RNA/DNA processes such as methylation, translation, and transcription (Figure 3B; Table S2).

Considering methyltransferases and m6a methylation as central players in cortical neurogenesis progression,[22] including its

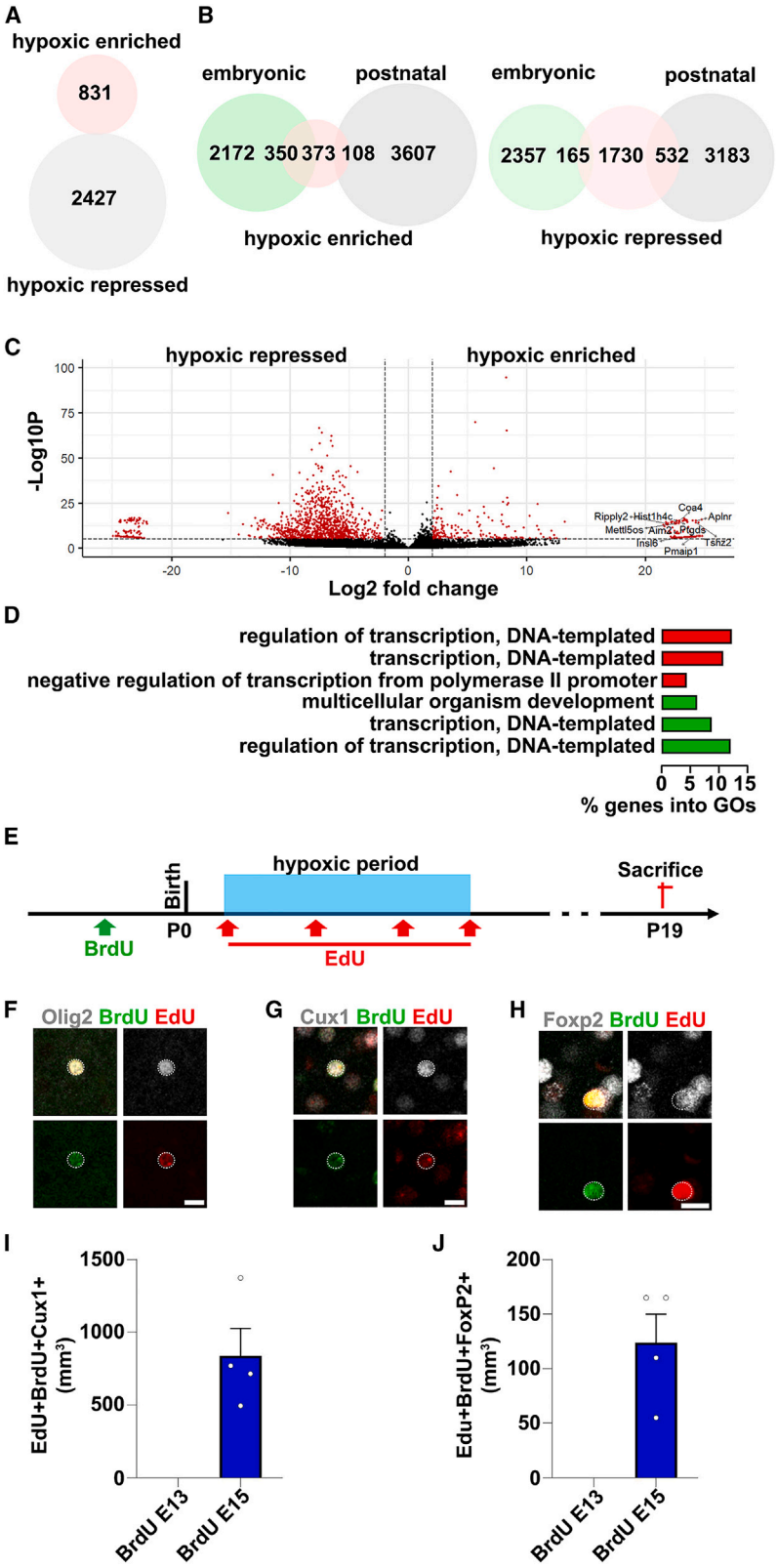

Figure 2. Hypoxia induces "embryonic transcriptional traits" within postnatal GLU progenitors

(A and B) Venn diagrams showing the number of differentially expressed genes (padj < 0.01) in GLU progenitors following hypoxia (A) as well as their comparison with embryonically or postnatally enriched transcripts in Nx mice (B).

(C) Volcano plot of transcripts repressed or enriched following hypoxia. Differentially expressed transcripts are in red (FC > 2 and p < 10e−6), while unchanged transcripts are in black. Annotated transcripts correspond to the top 50 enriched at embryonic vs. postnatal stages in Nx mice. Note that most are enriched following hypoxia, illustrating the acquisition of "embryonic traits" by postnatal GLU progenitors in this condition.

(D) Over-representation analysis of the top 1,000 enriched transcripts in embryonic (green) and Hx P12 GLU progenitors (red). Note the similarity of biological process categories.

(E) Schematic representations of the experimental procedure used in (F)–(J). BrdU was administrated at E13 or E15, while EdU was administrated at P3, P6, P9, and P11, corresponding to the period of hypoxia. Animals were sacrificed at P19.

(F–H) Representative immunostainings showing BrdU+/EdU+ cells expressing the oligodendroglial marker Olig2 (F) or the glutamatergic markers Cux1 (upper layer, G) or Foxp2 (deeper layer, H). Scale bars: 10 μm.

(I and J) Bar plots showing the density of hypoxia-induced Cux1+ and Fopx2 neurons. Note that these neurons are exclusively observed following E15 BrdU injection, indicating that they originate from later-cycling progenitors (N ≥ 4).

Data are presented as mean ± SEM. GO, Gene Ontology; P0 and P19, 0 and 19 days after birth, respectively; E13 and E15, 13 and 19 embryonic days, respectively.

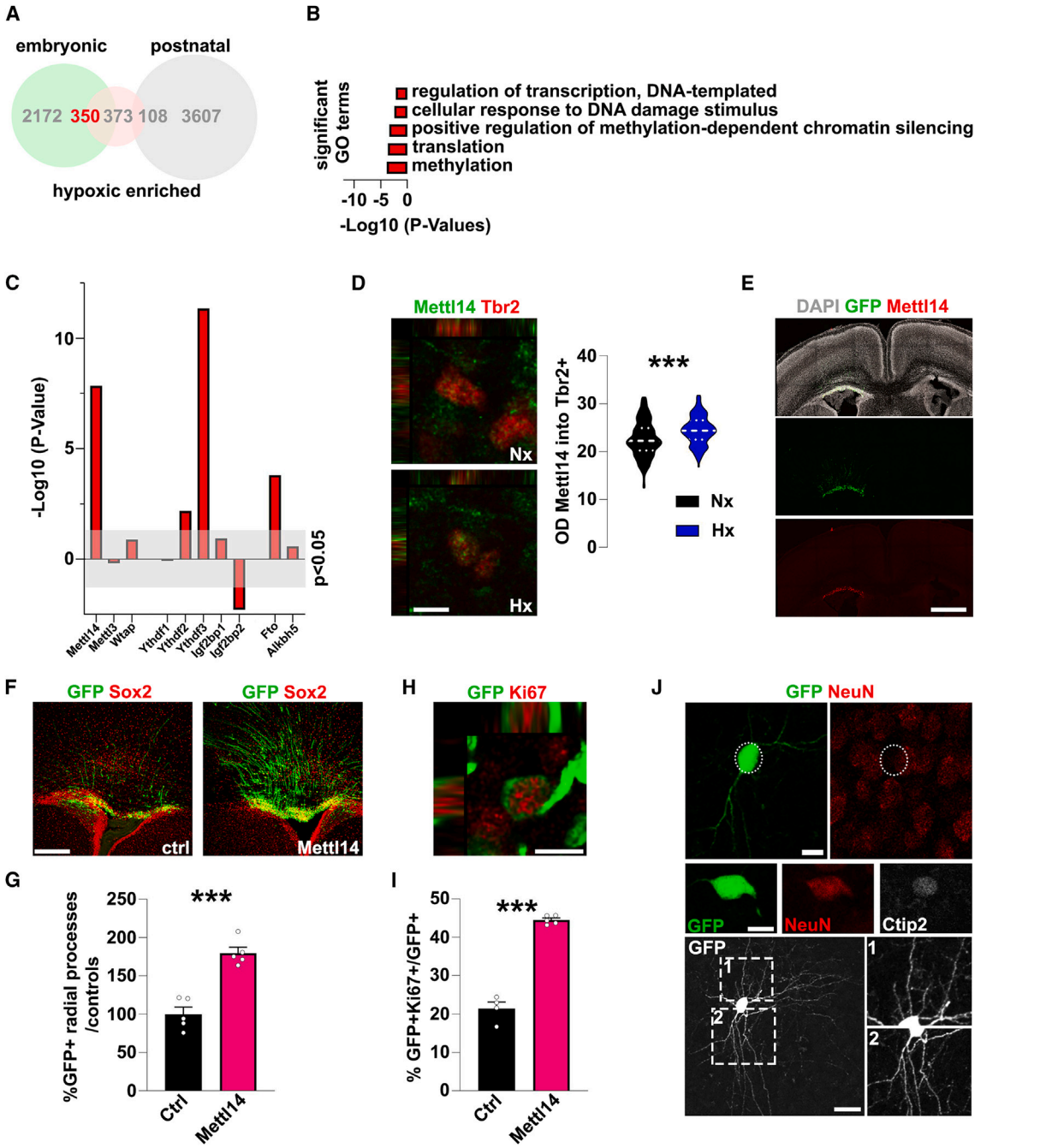

Figure 3. Hypoxia-induced upregulation of Mettl14 expression promotes postnatal NSC activation and cortical neurogenesis

(A) Venn diagrams highlighting (red) the number of transcripts commonly expressed in GLU progenitors during embryogenesis and induced by hypoxia (padj < 0.01).

(B) Related biological processes identified by over-representation analysis. Results underline a role of methylation in the response of GLU progenitors to hypoxia.

(C) Bar plot showing up- and downregulation of m6a-signaling transcripts in GLU progenitors following hypoxia, based on p values.

(D) Illustrations and violin plot of Mettlt14 optical density in GLU progenitors (Tbr2+) at P13, revealing its upregulation following hypoxia (N ≥ 4). Scale bar: 10 μm.

(E–G) Postnatal electroporation results in a rapid (48 h) and pronounced overexpression of Mettl14 detected by immunostaining within the dV-SVZ (E). Illustrations (F) and quantifications (G) showing the maintenance of NSCs (radial glial cell [RGC]-like morphology cells) into the dV-SVZ following an electroporation of mettl14 plasmid at 4 dpe (N ≥ 4). Scale bars: 500 and 200 μm.

(H and I) Illustration (H) and bar plot (I) showing the expression of Ki67 marker into GFP+ cells and its increase following mettl14 gain-of-function into the dV-SVZ at 4 dpe (N ≥ 4). Scale bar: 10 μm.

(legend continued on next page)

rapid decline at postnatal stages,[5] we next focused on the expression of these enzymes following hypoxia. Interestingly, hypoxia resulted in the upregulation of several methyltransferase transcripts in cortical progenitors, the most prominent being *Mettl14* (Figure 3C). This result was confirmed at protein level by performing a quantification of the optical density of Mettl14 staining into Tbr2+ progenitors (Figure 3D). Remarkably, other components of m6a signaling were also upregulated by hypoxia, including Ythdf2 and -3 (Figure 3C), which are known to promote mRNA decay.[23] These results suggest an important role for posttranscriptional regulation in promoting hypoxia-induced cortical neurogenesis and prompted us to investigate the effect of Mettl14 postnatal (P1) overexpression in mimicking some of the observations made following chronic hypoxia. Successful overexpression of Mettl14 was confirmed at 2 days post-electroporation (dpe) by immunostaining (Figure 3E). At 4 dpe, we observed in the dV-SVZ a persistence of radial glial cell-like cells (i.e., NSCs; Figures 3F and 3G), as well as an increased proliferation (GFP+/Ki67+; Figures 3H and 3I), similar to that observed following hypoxia (see above). Interestingly, electroporated cells with neuronal morphologies were again observed within the cortex of these animals at longer time points (i.e., P19) into both upper and deeper layers. However, only a fraction (<10%) expressed mature neuronal markers (i.e., NeuN, Ctip2, Cux1). Further, they failed to show dendritic spines as well as branched axons and GFP swellings (Figure 3J), indicating that Mettl14 gain-of-function alone is not sufficient to fully recapitulate the effects of chronic hypoxia.

Activation of the Wnt canonical pathway promotes cellular differentiation following hypoxia

Other pathways are likely to act in concert with methylation modifications to drive hypoxia-induced cortical neurogenesis. The Wnt canonical pathway is, in this context, of particular interest. Indeed, previous work has demonstrated a role of the Wnt canonical pathway in promoting postnatal cortical neurogenesis,[5,21,24] as well as in driving the competence of cortical progenitors to generate deep cortical neuron subtypes.[25] We used the Wnt/β-catenin reporter mouse (i.e., β-catenin/TCF/LEF reporter transgenic mice, also named BatGal mice),[26] to monitor activity of this signaling pathway during development and confirmed a gradual decline of its activity from E13 to P1 within the pallium and dV-SVZ (Figures S4A and S4B). Interestingly, chronic hypoxia resulted in a significant increase of beta-galactosidase (βGal) expression within the dV-SVZ at P11 (Figures 4A and 4B), indicating that reactivation of canonical Wnt signaling parallels the increased germinal activity observed following chronic hypoxia. At the transcriptional level, these changes of activity were paralleled by increased expression of transcripts coding for Wnt activators (e.g., *Lrp6*, *Dvl2*), while inhibitors were downregulated (*Sfrp5, Axin1*; Figure 4C) within GLU progenitors. Interestingly, overexpression of Mettl14 by electroporation at P1 in BatGal transgenic mice resulted in increased βGal expression at 2 dpe (Figures 4D and 4E), suggesting that both pathways act in synergy.

We used a previously established pharmacological strategy to promote the activity of Wnt canonical pathway (intranasal delivery of the GSK3β inhibitor CHIR99021 [CHIR])[21] following hypoxia. We confirmed that CHIR intranasal administration resulted in a further increase of canonical Wnt signaling activity within the dV-SVZ of BatGal mice (Figures 4F and 4G). This increase of Wnt/β-catenin activity was confirmed to occur within both glutamatergic and oligodendroglial progenitors (Tbr2+ and Olig2+, respectively; Figures 4F, 4H, and 4I). To investigate the consequence of this treatment following hypoxia, we labeled dV-SVZ NSCs by electroporation at P1 and investigated the fate of their progeny at P19 and P45. We confirmed the presence of GFP+ neurons within the cortex of both treated and untreated hypoxic mice at P19. Interestingly, CHIR treatment resulted in a higher proportion of GFP+ neurons expressing the cortical glutamatergic markers Cux1+ and Ctip2+ (Figure 4J). The larger proportion of GFP+ neurons expressed the deep-layer marker Ctip2 (47%), with morphological analyses showing a marked complexification of their dendritic arbors (Figures 4K, 4L, and S4E). Thus, CHIR treatment promotes acquisition of deep cortical layer markers, as well as the maturation of hypoxia-induced neurons. Interestingly, the effects of CHIR were not restricted to neurogenesis but also encompassed oligodendrogenesis. Indeed, while hypoxia resulted in a blockade of oligodendrocytes maturation at P19, as previously reported,[19] the delay of oligodendrocyte maturation were restored by CHIR treatment. We used cell morphology and select marker expression to assess oligodendrocyte lineage maturation (Figures 4M, S4C, and S4D). CHIR treatment allowed a recovery of mature oligodendroglial morphologies at P19 (Figures 4M and 4N), as well as of CC1+/Olig1^{cytoplasmic}+ expression (Figure 4O). Further, the persistent decreased expression of the myelinating marker GSTpi observed at P45 following hypoxia was also partially recovered by the treatment (Figure 4P).

Taken together, these results demonstrate that Wnt/β-catenin signaling pathway activation not only enhances oligodendrogenesis and neurogenesis following hypoxia, as previously reported,[21] but also promotes the differentiation and maturation of these two neural cell types.

CHIR treatment does not deplete the reservoir of young adult V-SVZ NSCs

Together, our results highlight a role for dorsal NSCs and progenitors in participating in the spontaneous regenerative attempt occurring following neonatal chronic hypoxia, as well as their amenability to pharmacological manipulation. We next assessed the impact of such manipulation onto V-SVZ NSC number and/or activity following hypoxia. Recent studies have highlighted the coexistence of subtypes of NSCs defined by their activation stage, which numbers and dynamics allow the maintenance of V-SVZ germinal activity throughout life.[27,28] We combined label-retaining protocols and cell-cycle stainings to distinguish four stages of NSC activation, i.e., quiescent, transiently active, active, and proliferative NSCs (Figures 5A and 5B). Quiescent NSCs

(J) Illustrations of neuron-like cells observed into the cortical area following mettl14 gain of function at 18 dpe. Only 10% of those neuron-like cells express mature neuronal markers (NeuN or Cux1 or Ctip2; left) and fail to arbor dendritic spines and axonal swellings. Scale bars: 10 and 20 μm.

***p < 0.001; statistical tests: statistical analysis was performed through parametric unpaired t test. Data are presented as mean ± SEM and as median and quartile for (D). GO, Gene Ontology; OD, optical density; Nx, normoxic; Hx, hypoxic; ctrl, control.

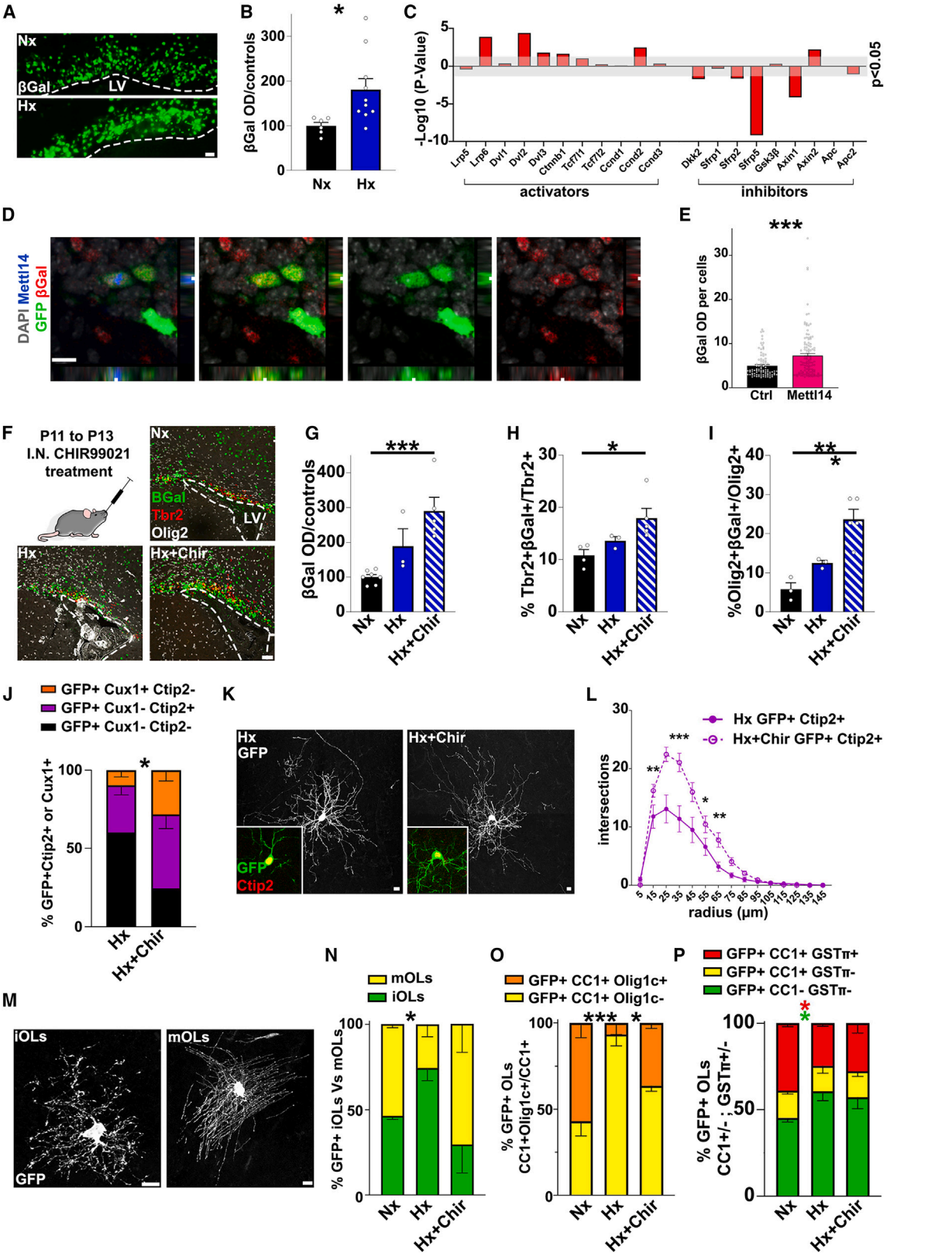

(legend on next page)

(qNSCs) were labeled by a single BrdU or EdU injection at E14.[29] Quantification of qNSCs at different time points confirmed their gradual recruitment during postnatal life, as previously described[27] (Figure S5A). The vast majority of qNSCs were negative for the proliferation marker MCM2 (<3%; Figures S5B and S5C) and only minimally overlapped (<6.5%) with transiently active NSCs (taNSCs) marked by using a chronic BrdU chasing protocol[30] (Figures S5D and S5E). Half of this later population expressed MCM2, reflecting their transiently active nature (Figures S5F and S5G). Importantly, both populations expressed the stem cell marker Sox2 but not the ependymal cell marker S100β. Quantification revealed that both qNSCs and taNSCs were not depleted following CHIR administration (Figures 5C–5E).

We complemented those quantifications by staining active and proliferative NSCs (aNSCs and pNSCs, respectively), which were positive for the cell-cycle marker MCM2 alone (Sox2+/MCM2+/Ki67−) or in combination with Ki67 (Sox2+/MCM2+/Ki67+), respectively[31] (Figures 5A and 5B). Our results reveal an absence of effects of chronic hypoxia and CHIR treatment on aNSC numbers (Figure 5F), while no significant increase of pNSC number was observed (Figure 5G). Because the Wnt pathway is mostly active within the dV-SVZ, we performed additional quantifications within this domain. This analysis revealed a marked proliferative effect of CHIR treatment until P45 within the dV-SVZ, with quantifications at P90 revealing a progressive return to baseline (Figures S5H and S5I). In agreement, BrdU treatment from P45 to P60 revealed an increased neurogenesis within the olfactory bulb at P90, whereas quantification of immature Dcx+ neurons at this late time point confirmed a progressive return to physiological neurogenesis levels (Figures 5H and 5I).

Together, these results indicate that short-term CHIR treatment following hypoxia results in long-lasting increased germinal activity of the V-SVZ, which, however, gradually returns to baseline and does not lead to NSC depletion.

DISCUSSION

In the present study, we used a neonatal chronic hypoxia model to assess the competence of postnatal NSCs to participate in cortical repair. We focus our analyses on NSCs of the dV-SVZ, which derives from the embryonic pallium. We demonstrate the capacity of postnatal NSCs to produce diverse subtypes of cortical cells, including neurons expressing upper- and deep-layer markers. We explored the mechanisms that parallel this response by performing a transcriptomic analysis of glutamatergic progenitors using the Neurog2Ai14$^{CreERT2/TdTomato}$ mice. Our results highlight a profound modulation of m6a and Wnt/β-catenin signaling in hypoxic conditions. A pharmacological activation of Wnt/β-catenin signaling promotes hypoxia-induced neuron and oligodendrocyte maturation, with no long-term impact on V-SVZ NSC germinal activity.

The targeted electroporation approach used in this study allows the selective and permanent labeling of NSCs residing in defined V-SVZ domains.[32] A direct comparison of NSCs residing within the dorsal and lateral domains of the postnatal V-SVZ revealed the competence of postnatal dV-SVZ NSCs to produce cortical cells postnatally when compared to those of the lateral domain. Further, these experiments demonstrate that dV-SVZ NSCs have the competence to produce both glial and neuronal cells within the cortex, including neurons expressing defined cortical layer markers (e.g., Cux1, Ctip2, Foxp2). These results are in line with original studies reporting a secondary cortical neurogenesis, including glutamatergic neurons[20] and oligodendrocytes,[19] following neonatal chronic hypoxia. Our results support a direct contribution of dV-SVZ NSCs to this regenerative response, in line with our previous demonstration of the persistence of glutamatergic progenitors within this postnatal region.[5] It should, however, be noted that the number of newborn neurons remains low in comparison to previous studies. Indeed, both our fate mapping and BrdU staining suggest that the number of newborn neurons remains marginal (<0.1% of the total number of cortical neurons), contrasting with the >40,000 neurons observed in previous studies.[18] Thus, although our electroporation approach probably underestimates the number of newborn neurons, due to incomplete targeting of the NSC population, it is very unlikely that such a large number of neurons is generated following chronic hypoxia. Most of the previously observed BrdU+ newborn neurons could come from misinterpretation due to intense labeling of satellite cells at these early postnatal stages.

Figure 4. Wnt pathway activation promotes the differentiation of neurons into glutamatergic lineage and oligodendrocyte lineage maturation

(A and B) Illustrations (A) and bar plot (B) showing the optical density measurement of beta-galactosidase expression in dV-SVZ at P11 in the BatGal reporter mice. Results show its upregulation following hypoxia ($N \geq 6$). Scale bar: 20 μm.

(C) Bar plot showing up- and downregulation of canonical Wnt-signaling transcripts in GLU progenitors following hypoxia, based on p values.

(D and E) Illustration (D) and bar plot (E) showing the increased beta-galactosidase optical density 2 days following overexpression of Mettl14 at P1 in the BatGal reporter mice ($N \geq 4$). Scale bar: 10 μm.

(F–I) Illustrations (D) and bar plots (E–G) showing the return to baseline of Wnt pathway activity by P15 following hypoxia into dV-SVZ (D and E) and in both progenitor populations, glutamatergic (Tbr2+; D and F) and oligodendrocyte (Olig2+; D and G). CHIR99021 treatment prolonged the Wnt activity and potentiated it (D–G) ($N \geq 3$). Scale bar: 50 μm.

(J) Bar plot showing that CHIR99021 treatment increases the proportion of the newborn neurons expressing cortical-specific mature glutamatergic markers ($N \geq 6$).

(K and L) Illustrations (K) and bar plot (L) of morphological analyses of deeper GFP+Ctip2+ neurons. Results show a complexification in the CHIR99021-treated group as shown by Sholl ($n \geq 10$). Scale bar: 10 μm.

(M and N) Immature and mature GFP+ oligodendrocytes can be distinguished based on their morphology (M). Hypoxia results in a reduction in the acquisition of mature morphologies, which was fully rescued by CHIR99021 treatment (N) ($N \geq 5$). Scale bar: 10 μm.

(O and P) Oligodendrocyte lineage maturation can be distinguished based on marker expressions (see Figures S5C and S5D). Hypoxia results in a reduction in the acquisition of mature markers such as Olig1 into the cytoplasm (O) or GSTpi (P), which was rescued by CHIR99021 treatment ($N \geq 4$).

*$p < 0.05$, **$p < 0.01$, and ***$p < 0.001$. Data are presented as mean ± SEM; statistical tests: statistical analysis was performed through parametric unpaired t test for (A) and (E), one-way ANOVA followed by Bonferroni post hoc test for (G)–(I), and two-way ANOVA followed by Bonferroni post hoc test for (J), (L), (N), and (P). OD, optical density; Nx, normoxic; Hx, hypoxic; IN, intranasal; Chir, CHIR99021; iOLs, immature oligodendrocytes; mOLs, mature oligodendrocytes.

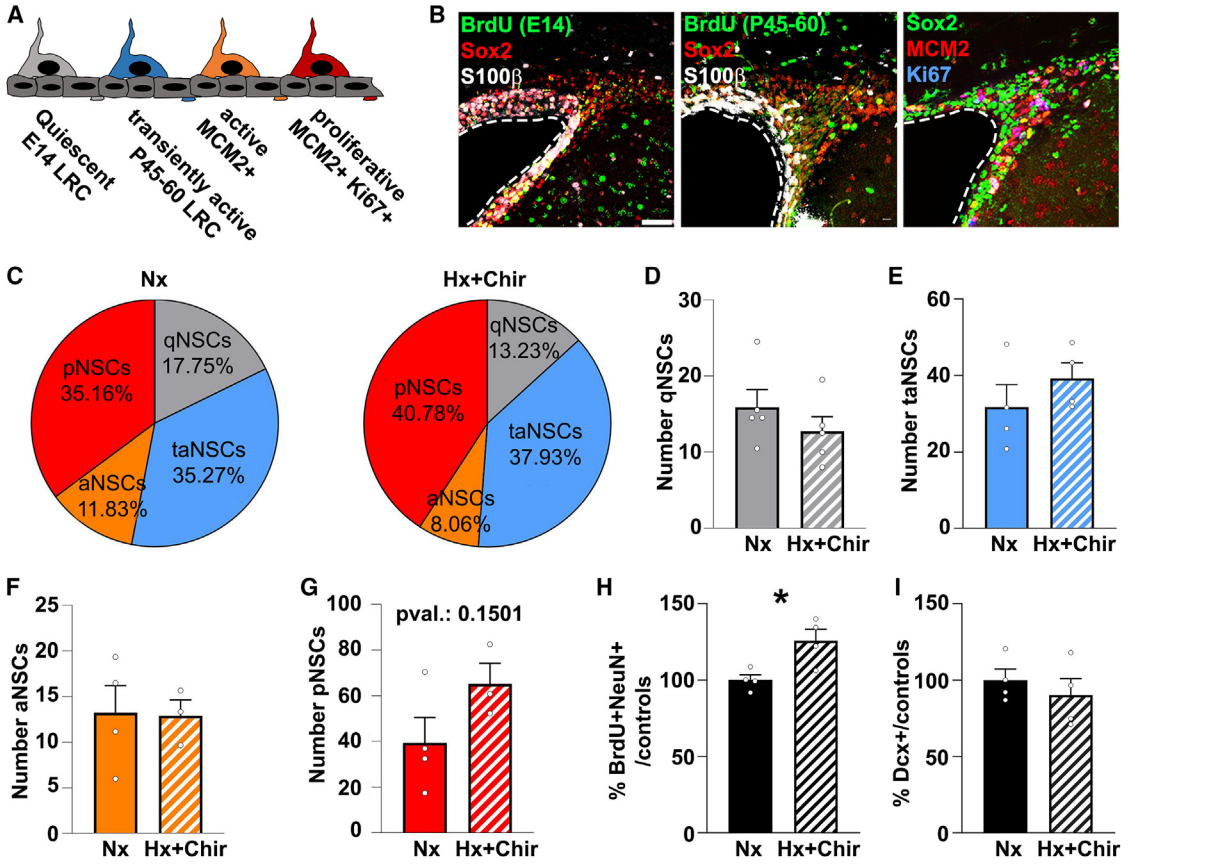

Figure 5. CHIR99021 treatment does not impact young adult germinal activity, nor NSC pools

(A) Schematic representation of subtypes of NSCs and their marker expressions corresponding to label-retaining cell (LRC) protocols and their cell-cycle marker expression.

(B) Illustrations of NSC subtypes, qNSCs (i.e., Sox2$^+$ BrdUE14bright$^+$ S100β$^-$; left), taNSCs (i.e., Sox2$^+$ BrdUP45-60$^+$ S100β$^-$; middle), and aNSCs and pNSCs (i.e., Sox2$^+$ MCM2$^+$ and Sox2$^+$ MCM2$^+$ Ki67$^+$; right). Scale bar: 50 μm.

(C–G) Quantifications reveal the absence of dramatic modifications of the percentage (C) and raw number per section in V-SVZ of qNSC (D), taNSC (E), aNSC (F), and pNSC (G) populations at P45 following hypoxia and CHIR99021 treatment (N ≥ 3).

(H) Quantification of neuronal production in the olfactory bulbs between P45 and P60 (BrdU$^+$ cells) confirms the increase of cell production at P45 (N ≥ 4).

(I) Quantification of neuroblasts (DCX$^+$ cells) in olfactory bulbs at longer time points (i.e., P90), indicating a return to physiological level of neuronal production by P90 (N ≥ 4).

*p < 0.05. Data are presented as mean ± SEM; statistical tests: statistical analysis was performed through parametric unpaired t test for (D)–(I). LRC, label-retaining cell; qNSCs, quiescent neural stem cells; taNSCs, transiently active neural stem cells; aNSCs, active neural stem cells; pNSCs, proliferative neural stem cells; Nx, normoxic; Hx, hypoxic; Chir, CHIR99021.

However, despite their limited numbers, the observation of cortical neurons, including some expressing deep-layer markers, is remarkable. This observation suggests that the postnatal dV-SVZ remains competent to produce cortical neurons, which are normally produced at early embryonic times. Cortical progenitors have long been thought to gradually lose this competence during development. For instance, original heterochronic transplantation experiments of late-cycling progenitors into the early embryonic ferret V-SVZ showed that they are committed to generating upper-layer neurons.[33] This view was, however, recently challenged by the demonstration of the competence of late pallial NSCs to produce deep-layer cortical neurons when exposed to an earlier-stage environment.[25,34] Further, V-SVZ explants from postnatal dV-SVZ (P9–P11) and adult (3-month-old) brains produce cortical pyramidal neurons when cocultured with embryonic sections.[16] However, at neonatal ages, a mix of aNSCs and qNSCs are present within the dV-SVZ.[6] Our results suggest a rejuvenation of competences of aNSCs and progenitors within the dV-SVZ or a delay of entry into quiescence of those rather than a reactivation of dorsal qNSCs. Indeed, the absence of BrdU+Cux1+ and Foxp2+ neurons following E13 BrdU injection (Figures 2E–2J) suggests that hypoxia does not recruit pools of qNSCs, which could conserve their competences over the quiescent state. Together, these results are in line with a persisting competence of late NSCs, including postnatal ones, to produce earlier-born neurons when exposed to appropriate signals, such as those resulting from neonatal chronic hypoxia.

Indeed, our results underline that this response is paralleled by transcriptional changes resulting in a "rejuvenation" of postnatal progenitors (i.e., the acquisition of a transcriptional signature

resembling those of embryonic progenitors). Interestingly, our results suggest a key role for oxygen tension in the induction of these transcriptional changes. Indeed, a low-oxygen environment defines the embryonic period,[35] and oxygenation is a key regulator of cellular behaviors.[36] Thus, *in vitro* low oxygenation promotes NSC proliferation and neurogenesis.[37,38] Oxidative stress is known to have multiple cellular consequences through the activation of several signaling pathways that allow organisms to adapt to a range of oxygen concentration (tensions).[39] More than 60 2-oxoglutarate oxygen-dependent dioxygenase enzymes continuously sense physiological changes in oxygen tension, among which is the well-characterized hypoxia-inducible factor pathway.[40] Those oxygen-sensing enzymes act onto transcription, either directly by target gene promoter binding or indirectly by epigenetic modifications, including histone and DNA methylation.[41–43] Future studies will be required to investigate the mechanisms linking hypoxia to postnatal NSC activation/rejuvenation.

Our transcriptional analysis supports a key role for m6a signaling in the hypoxia-induced regenerative response. m6a modification is the most abundant mRNA modification in eukaryotic cells.[44] It plays a central role as posttranscriptional regulator during mammalian development and is involved in numerous biological processes such as stem cell maintenance, proliferation, and fate decisions.[45,46] In addition, it is now clear that m6a methylation participates in the maintenance of NSCs,[47] as well as in NSC temporal competence progression.[22] Indeed, Mettl14 conditional knockout at early embryonic times delays embryonic neurogenesis,[22] while its downregulation parallels cortical glutamatergic neurogenesis closure around birth.[5] It is tempting to speculate that this effect is at least partially mediated by a modification of radial glia proliferation. Indeed, *Mettl14*$^{-/-}$ radial glia exhibit prolonged cell-cycle progression,[22] while in our experiments, hypoxia induces an increase Mettl14 expression, with both hypoxia and Mettl14 OE inducing an increase of proliferation within the dV-SVZ. Thus, even if Mettl14 overexpression appears not to be sufficient to fully reproduce the regenerative response observed following chronic hypoxia, it phenocopied some aspects of this response, including the increased proliferation, persistence of radial processes, and migration of GFP+ cells presenting a neuronal morphology within the cortex.

The concomitant activation by chronic hypoxia of the Wnt canonical pathway observed in our analysis suggests possible links between these two signaling pathways. Recent evidence suggests a regulation of Wnt/β-catenin signaling by m6a methylation in other tissues. Indeed, in intestinal cells, Ythdf1 deletion dramatically blocks Wnt/β-catenin activity, suggesting the regulation of canonical Wnt/TCF signaling in an m6a-methylation-dependent manner.[48] Further, a reduction of Wnt signaling activity is paralleled by a reduction of DNA methylation in mouse embryonic stem cells.[49] Finally, a correlation is observed between m6a tags and expression of transcripts related to the Wnt/β-catenin signaling pathway in NSCs.[5,22] Thus, it is tempting to speculate that m6a and Wnt/β-catenin signaling act in parallel and regulate each other to control pallial NSC competence over time, in health as well as following injury.

Interestingly, our observation of a spontaneous reactivation of Wnt/β-catenin signaling following chronic hypoxia in the dV-SVZ is in line with previous studies linking activation of this signaling pathway to NSC proliferation and oxygen tension.[37,50,51] We used a pharmacological approach, i.e., intranasal administration of CHIR to inhibit Gsk3β and thus promote Wnt/β-catenin activity within the dV-SVZ NSCs,[52–54] in line with our previous work.[21,24,55] Interestingly, CHIR treatment promoted the generation of cortical neurons expressing the deep-layer marker Ctip2, suggesting an increased capacity of NSCs to produce early-born neuron subtypes upon Wnt/β-catenin signaling activation. These results are in agreement with the observed decrease of Wnt/β-catenin activity within the pallium during embryonic development, while the sequential production of cortical glutamatergic neurons unfold (see Figure S4).[56,57] They are also in line with the observation that *in vitro* exposure of late (E14.5) cortical progenitors to CHIR promotes their competence to produce deep-layer neurons once transplanted in E12.5 embryos.[25] Thus, although mechanisms remain unknown, these observations converge in associating Wnt-pathway activation with the production of deep-layer neurons by cortical progenitors. These data indicate an essential role of Wnt signaling as an evolutive extrinsic factor triggering cortical neurogenesis in a stage-specific manner and suggest that a low level of Wnt is primordial to the closure of pallial/dorsal germinal activity.[5] Together, those results highlight a key role for Wnt/β-catenin signaling in regulating pallial NSC glutamatergic neuronal competence over time, as well as in promoting *de novo* cortical neurogenesis and oligodendrogenesis following neonatal chronic hypoxia.

Accumulating evidence indicates that a tight regulation of the balance between NSC activity and quiescence must be maintained to allow the maintenance of postnatal and adult germinal activity. Further, the balance between canonical and non-canonical Wnt activity either promoting NSC activity[52,58] or quiescence[27], was shown to play a key role in germinal activity maintenance. In this context, it appeared crucial to investigate the effect of CHIR treatment on the reservoir of NSCs and their germinal activity. Importantly, our results using label-retaining protocols as well as various markers demonstrated that CHIR treatment does not induce depletion of the young adult NSC pool, nor their capacity to participate in olfactory bulb neurogenesis at this stage. This suggests an underappreciated capacity of V-SVZ NSCs to adapt to adverse conditions (i.e., injury, changes in signaling), possibly by changing the balance of symmetric vs. asymmetric divisions[59] or other mechanisms that compensate NSC activation, such as resting NSC mechanisms shown in the hippocampus to sustain adult germinal activity,[60,61] which remains to be fully explored within the V-SVZ.

Altogether, our work shows a discrete but significant capacity of postnatal V-SVZ NSCs to participate in cortical repair and underline their amenability and resilience to pharmacological manipulation.

Limitations of the study

Our results of a *de novo* cortical neurogenesis are in line with previous reports. However, as indicated in the discussion, we believe that the extent of this *de novo* neurogenesis is lower than previously reported.[18] It is important to note that due to technical reasons, it is also difficult to quantify accurately the extent of this neurogenesis: (1) the hypoxic period last 8 days and is followed by a period of 8 days of recovery, thus resulting in BrdU injections at select time points to only label a fraction of

these neurons. (2) Similarly, postnatal electroporations only label a fraction of NSCs, thus complicating the quantification of newborn neurons. Thus, because of similar technical limitations, we cannot firmly quantify the number of neurons produced following hypoxia, nor if all of these neurons originate from V-SVZ NSCs. It is also important to mention that in this study, we have not looked at the long-term survival of these neurons, nor at their functional integration, although the careful histology we have performed supports their integration and maturation. Although we demonstrated that inhibition of Gsk3β by intranasal CHIR administration activates the Wnt canonical pathway (see Figures 4F–4I), this drug also shows lower affinity to Gsk3α (Tocris, IC50 values are 6.7 and 10 nM for Gsk3β and Gsk3α, respectively), a potential role for which could be explored in future studies. Finally, although inhibition of the Wnt canonical pathway could have completed this study, we did not perform these experiments because of two technical limitations: (1) the number of newborn neurons is too low to appreciate a partial blockade of hypoxia-induced neurogenesis and (2) drugs that inhibit Wnt-signaling are not specific and/or have not yet been characterized *in vivo*.

STAR★METHODS

Detailed methods are provided in the online version of this paper and include the following:

- KEY RESOURCES TABLE
- RESOURCE AVAILABILITY
  - Lead contact
  - Materials availability
  - Data and code availability
- EXPERIMENTAL MODEL AND STUDY PARTICIPANT DETAILS
  - Animals
- METHOD DETAILS
  - In-vivo
  - Ex-vivo
- QUANTIFICATION AND STATISTICAL ANALYSIS
  - Animal and brain weights
  - Cortical volume
  - Dorsal V-SVZ area
  - Quantification of cell fate
- RESULTS PRESENTED AS RAW NUMBER OF CELLS *PER* SECTION
- RESULTS PRESENTED AS NUMBER OF CELLS *PER* VOLUME
- RESULTS PRESENTED AS PERCENTAGES OF CELL ON A CELLULAR POPULATION
- RESULTS PRESENTED AS PERCENTAGES OF CELL COMPARED TO CONTROL
- RESULTS PRESENTED AS PERCENTAGE OF CELLS
- RESULTS PRESENTED AS OPTICAL DENSITY MEASUREMENTS
  - Morphological analysis
  - Differential gene expression
  - Over representation analysis (ORA) & gene ontology (GO) analyses

SUPPLEMENTAL INFORMATION

Supplemental information can be found online at https://doi.org/10.1016/j.celrep.2024.113734.

ACKNOWLEDGMENTS

We are grateful to Corentin Place, Maxence Dubois, Alizé Colombat, and Alexane Andrieux for their help during their respective internships. We thank Priscillia Battiston-Montagne (cytometry platform of CRCL, Lyon) for her advice regarding cell sorting and Séverine Croze (genomic platform ProfileXpert, Lyon) for her expert help with bulk RNA sequencing. This work was funded by the French National Research Agency (ANR) NeoRepair (ANR-17-CE16-0009), ANR NeoReGen (ANR-22-CE17-0029), ANR Rewired (ANR-22-CE16-0019), and LABEX CORTEX (ANR-11-LABX-0042) of the "Université de Lyon" within the program "Investissements d'Avenir" (decision n° 2019-ANR1051 LABX-02) operated by the ANR.

AUTHOR CONTRIBUTIONS

Conceptualization, O.R.; methodology, O.R., C.P., G.M., and L.F.; software, L.F. and G.M.; investigation, L.F., T.C., D.A., C.L., V.D., and G.M.; writing – original draft, L.F. and O.R.; writing – review & editing, L.F., L.B., C.H., V.D., G.M., C.P., and O.R.; visualization, L.F. and O.R.; supervision, O.R. and G.M.; funding acquisition, O.R. and C.P.

DECLARATION OF INTERESTS

The authors declare no competing interests.

Received: May 31, 2023
Revised: November 3, 2023
Accepted: January 16, 2024
Published: February 13, 2024

REFERENCES

1. Molyneaux, B.J., Arlotta, P., Menezes, J.R.L., and Macklis, J.D. (2007). Neuronal subtype specification in the cerebral cortex. Nat. Rev. Neurosci. *8*, 427–437.
2. Kwan, K.Y., Šestan, N., and Anton, E.S. (2012). Transcriptional co-regulation of neuronal migration and laminar identity in the neocortex. Development *139*, 1535–1546.
3. Li, S., Mattar, P., Zinyk, D., Singh, K., Chaturvedi, C.-P., Kovach, C., Dixit, R., Kurrasch, D.M., Ma, Y.-C., Chan, J.A., et al. (2012). GSK3 Temporally Regulates Neurogenin 2 Proneural Activity in the Neocortex. J. Neurosci. *32*, 7791–7805.
4. Gao, P., Postiglione, M.P., Krieger, T.G., Hernandez, L., Wang, C., Han, Z., Streicher, C., Papusheva, E., Insolera, R., Chugh, K., et al. (2014). Deterministic Progenitor Behavior and Unitary Production of Neurons in the Neocortex. Cell *159*, 775–788.
5. Donega, V., Marcy, G., Lo Giudice, Q., Zweifel, S., Angonin, D., Fiorelli, R., Abrous, D.N., Rival-Gervier, S., Koehl, M., Jabaudon, D., and Raineteau, O. (2018). Transcriptional Dysregulation in Postnatal Glutamatergic Progenitors Contributes to Closure of the Cortical Neurogenic Period. Cell Rep. *22*, 2567–2574.
6. Marcy, G., Foucault, L., Babina, E., Capeliez, T., Texeraud, E., Zweifel, S., Heinrich, C., Hernandez-Vargas, H., Parras, C., Jabaudon, D., and Raineteau, O. (2023). Single-cell analysis of the postnatal dorsal V-SVZ reveals a role for Bmpr1a signaling in silencing pallial germinal activity. Sci. Adv. *9*, eabq7553.
7. Fiorelli, R., Azim, K., Fischer, B., and Raineteau, O. (2015). Adding a spatial dimension to postnatal ventricular-subventricular zone neurogenesis. Development *142*, 2109–2120.

8. Sequerra, E.B. (2014). Subventricular zone progenitors in time and space: generating neuronal diversity. Front. Cell. Neurosci. *8*, 434.
9. Kessaris, N., Fogarty, M., Iannarelli, P., Grist, M., Wegner, M., and Richardson, W.D. (2006). Competing waves of oligodendrocytes in the forebrain and postnatal elimination of an embryonic lineage. Nat. Neurosci. *9*, 173–179.
10. Naruse, M., Ishizaki, Y., Ikenaka, K., Tanaka, A., and Hitoshi, S. (2017). Origin of oligodendrocytes in mammalian forebrains: a revised perspective. J. Physiol. Sci. *67*, 63–70.
11. Qi, Y., Stapp, D., and Qiu, M. (2002). Origin and molecular specification of oligodendrocytes in the telencephalon. Trends Neurosci. *25*, 223–225.
12. Brill, M.S., Ninkovic, J., Winpenny, E., Hodge, R.D., Ozen, I., Yang, R., Lepier, A., Gascón, S., Erdelyi, F., Szabo, G., et al. (2009). Adult generation of glutamatergic olfactory bulb interneurons. Nat. Neurosci. *12*, 1524–1533.
13. Winpenny, E., Lebel-Potter, M., Fernandez, M.E., Brill, M.S., Götz, M., Guillemot, F., and Raineteau, O. (2011). Sequential generation of olfactory bulb glutamatergic neurons by Neurog2-expressing precursor cells. Neural Dev. *6*, 12–18.
14. Jinnou, H., Sawada, M., Kawase, K., Kaneko, N., Herranz-Pérez, V., Miyamoto, T., Kawaue, T., Miyata, T., Tabata, Y., Akaike, T., et al. (2018). Radial Glial Fibers Promote Neuronal Migration and Functional Recovery after Neonatal Brain Injury. Cell Stem Cell *22*, 128–137.e9.
15. Sequerra, E.B., Costa, M.R., Menezes, J.R.L., and Hedin-Pereira, C. (2013). Adult neural stem cells: plastic or restricted neuronal fates? Development *140*, 3303–3309.
16. Sequerra, E.B., Miyakoshi, L.M., Fróes, M.M., Menezes, J.R.L., Hedin-Pereira, C., and Hedin-Pereira, C. (2010). Generation of Glutamatergic Neurons from Postnatal and Adult Subventricular Zone with Pyramidal-Like Morphology. Cereb. Cortex *20*, 2583–2591.
17. Scafidi, J., Fagel, D.M., Ment, L.R., and Vaccarino, F.M. (2009). Modeling premature brain injury and recovery. Int. J. Dev. Neurosci. *27*, 863–871.
18. Fagel, D.M., Ganat, Y., Silbereis, J., Ebbitt, T., Stewart, W., Zhang, H., Ment, L.R., and Vaccarino, F.M. (2006). Cortical neurogenesis enhanced by chronic perinatal hypoxia. Exp. Neurol. *199*, 77–91.
19. Salmaso, N., Jablonska, B., Scafidi, J., Vaccarino, F.M., and Gallo, V. (2014). Neurobiology of premature brain injury. Nat. Neurosci. *17*, 341–346.
20. Fagel, D.M., Ganat, Y., Cheng, E., Silbereis, J., Ohkubo, Y., Ment, L.R., and Vaccarino, F.M. (2009). *Fgfr1* Is Required for Cortical Regeneration and Repair after Perinatal Hypoxia. J. Neurosci. *29*, 1202–1211.
21. Azim, K., Angonin, D., Marcy, G., Pieropan, F., Rivera, A., Donega, V., Cantù, C., Williams, G., Berninger, B., Butt, A.M., and Raineteau, O. (2017). Pharmacogenomic identification of small molecules for lineage specific manipulation of subventricular zone germinal activity. PLoS Biol. *15*, e2000698.
22. Yoon, K.-J., Ringeling, F.R., Vissers, C., Jacob, F., Pokrass, M., Jimenez-Cyrus, D., Su, Y., Kim, N.-S., Zhu, Y., Zheng, L., et al. (2017). Temporal Control of Mammalian Cortical Neurogenesis by m6A Methylation. Cell *171*, 877–889.e17.
23. Wang, X., Zhao, B.S., Roundtree, I.A., Lu, Z., Han, D., Ma, H., Weng, X., Chen, K., Shi, H., and He, C. (2015). N6-methyladenosine Modulates Messenger RNA Translation Efficiency. Cell *161*, 1388–1399.
24. Azim, K., Fischer, B., Hurtado-Chong, A., Draganova, K., Cantù, C., Zemke, M., Sommer, L., Butt, A., and Raineteau, O. (2014). Persistent Wnt/β-Catenin Signaling Determines Dorsalization of the Postnatal Subventricular Zone and Neural Stem Cell Specification into Oligodendrocytes and Glutamatergic Neurons. Stem Cell. *32*, 1301–1312.
25. Oberst, P., Fièvre, S., Baumann, N., Concetti, C., Bartolini, G., and Jabaudon, D. (2019). Temporal plasticity of apical progenitors in the developing mouse neocortex. Nature *573*, 370–374.
26. Maretto, S., Cordenonsi, M., Dupont, S., Braghetta, P., Broccoli, V., Hassan, A.B., Volpin, D., Bressan, G.M., and Piccolo, S. (2003). Mapping Wnt/β-catenin signaling during mouse development and in colorectal tumors. Proc. Natl. Acad. Sci. USA *100*, 3299–3304.
27. Kalamakis, G., Brüne, D., Ravichandran, S., Bolz, J., Fan, W., Ziebell, F., Stiehl, T., Catalá-Martinez, F., Kupke, J., Zhao, S., et al. (2019). Quiescence Modulates Stem Cell Maintenance and Regenerative Capacity in the Aging Brain. Cell *176*, 1407–1419.e14.
28. Llorens-Bobadilla, E., Zhao, S., Baser, A., Saiz-Castro, G., Zwadlo, K., and Martin-Villalba, A. (2015). Single-Cell Transcriptomics Reveals a Population of Dormant Neural Stem Cells that Become Activated upon Brain Injury. Cell Stem Cell *17*, 329–340.
29. Fuentealba, L.C., Rompani, S.B., Parraguez, J.I., Obernier, K., Romero, R., Cepko, C.L., and Alvarez-Buylla, A. (2015). Embryonic Origin of Postnatal Neural Stem Cells. Cell *161*, 1644–1655.
30. Furutachi, S., Miya, H., Watanabe, T., Kawai, H., Yamasaki, N., Harada, Y., Imayoshi, I., Nelson, M., Nakayama, K.I., Hirabayashi, Y., and Gotoh, Y. (2015). Slowly dividing neural progenitors are an embryonic origin of adult neural stem cells. Nat. Neurosci. *18*, 657–665.
31. Codega, P., Silva-Vargas, V., Paul, A., Maldonado-Soto, A.R., DeLeo, A.M., Pastrana, E., and Doetsch, F. (2014). Prospective Identification and Purification of Quiescent Adult Neural Stem Cells from Their In Vivo Niche. Neuron *82*, 545–559.
32. Fernández, M.E., Croce, S., Boutin, C., Cremer, H., and Raineteau, O. (2011). Targeted electroporation of defined lateral ventricular walls: a novel and rapid method to study fate specification during postnatal forebrain neurogenesis. Neural Dev. *6*. 13–12.
33. Frantz, G.D., and McConnell, S.K. (1996). Restriction of Late Cerebral Cortical Progenitors to an Upper-Layer Fate. Neuron *17*, 55–61.
34. Donega, V., and Raineteau, O. (2017). Postnatal Neural Stem Cells: Probing Their Competence for Cortical Repair. Neuroscientist *23*, 605–615.
35. Torres-Cuevas, I., Parra-Llorca, A., Sánchez-Illana, A., Nuñez-Ramiro, A., Kuligowski, J., Cháfer-Pericás, C., Cernada, M., Escobar, J., and Vento, M. (2017). Oxygen and oxidative stress in the perinatal period. Redox Biol. *12*, 674–681.
36. Yun, K., Potter, S., and Rubenstein, J.L. (2001). Gsh2 and Pax6 play complementary roles in dorsoventral patterning of the mammalian telencephalon. Development *128*, 193–205.
37. Braunschweig, L., Meyer, A.K., Wagenführ, L., and Storch, A. (2015). Oxygen regulates proliferation of neural stem cells through Wnt/β-catenin signalling. Mol. Cell. Neurosci. *67*, 84–92.
38. Ortega, J.A., Sirois, C.L., Memi, F., Glidden, N., and Zecevic, N. (2017). Oxygen Levels Regulate the Development of Human Cortical Radial Glia Cells. Cereb. Cortex *27*, 3736–3751.
39. Kaelin, W.G., and Ratcliffe, P.J. (2008). Oxygen Sensing by Metazoans: The Central Role of the HIF Hydroxylase Pathway. Mol. Cell *30*, 393–402.
40. Melvin, A., and Rocha, S. (2012). Chromatin as an oxygen sensor and active player in the hypoxia response. Cell. Signal. *24*, 35–43.
41. Batie, M., Frost, J., Frost, M., Wilson, J.W., Schofield, P., and Rocha, S. (2019). Hypoxia induces rapid changes to histone methylation and reprograms chromatin. Science *363*, 1222–1226.
42. Chakraborty, A.A., Laukka, T., Myllykoski, M., Ringel, A.E., Booker, M.A., Tolstorukov, M.Y., Meng, Y.J., Meier, S.R., Jennings, R.B., Creech, A.L., et al. (2019). Histone demethylase KDM6A directly senses oxygen to control chromatin and cell fate. Science *363*, 1217–1222.
43. Chawla, R.K., Watson, W.H., and Jones, D.P. (1996). Effect of hypoxia on hepatic DNA methylation and tRNA methyltransferase in rat: Similarities to effects of methyl-deficient diets. J. Cell. Biochem. *61*, 72–80.
44. Jia, G., Fu, Y., and He, C. (2013). Reversible RNA adenosine methylation in biological regulation. Trends Genet. *29*, 108–115.
45. Cao, G., Li, H.-B., Yin, Z., and Flavell, R.A. (2016). Recent advances in dynamic m6A RNA modification. Open Biol. *6*, 160003.
46. Zhao, B.S., Roundtree, I.A., and He, C. (2017). Post-transcriptional gene regulation by mRNA modifications. Nat. Rev. Mol. Cell Biol. *18*, 31–42.

47. Wang, Y., Li, Y., Yue, M., Wang, J., Kumar, S., Wechsler-Reya, R.J., Zhang, Z., Ogawa, Y., Kellis, M., Duester, G., and Zhao, J.C. (2018). N6-methyladenosine RNA modification regulates embryonic neural stem cell self-renewal through histone modifications. Nat. Neurosci. *21*, 195–206.

48. Han, B., Yan, S., Wei, S., Xiang, J., Liu, K., Chen, Z., Bai, R., Sheng, J., Xu, Z., and Gao, X. (2020). YTHDF 1-mediated translation amplifies Wnt-driven intestinal stemness. EMBO Rep. *21*, e49229.

49. Theka, I., Sottile, F., Cammisa, M., Bonnin, S., Sanchez-Delgado, M., Di Vicino, U., Neguembor, M.V., Arumugam, K., Aulicino, F., Monk, D., et al. (2019). Wnt/β-catenin signaling pathway safeguards epigenetic stability and homeostasis of mouse embryonic stem cells. Sci. Rep. *9*, 948.

50. Cui, X.-P., Xing, Y., Chen, J.-M., Dong, S.-W., Ying, D.-J., and Yew, D.T. (2011). Wnt/beta-catenin is involved in the proliferation of hippocampal neural stem cells induced by hypoxia. Ir. J. Med. Sci. *180*, 387–393.

51. Mazumdar, J., O'Brien, W.T., Johnson, R.S., LaManna, J.C., Chavez, J.C., Klein, P.S., and Simon, M.C. (2010). O2 regulates stem cells through Wnt/β-catenin signalling. Nat. Cell Biol. *12*, 1007–1013.

52. Adachi, K., Mirzadeh, Z., Sakaguchi, M., Yamashita, T., Nikolcheva, T., Gotoh, Y., Peltz, G., Gong, L., Kawase, T., Alvarez-Buylla, A., et al. (2007). β-Catenin Signaling Promotes Proliferation of Progenitor Cells in the Adult Mouse Subventricular Zone. Stem Cell. *25*, 2827–2836.

53. Hirota, Y., Sawada, M., Huang, S.H., Ogino, T., Ohata, S., Kubo, A., and Sawamoto, K. (2016). Roles of Wnt Signaling in the Neurogenic Niche of the Adult Mouse Ventricular–Subventricular Zone. Neurochem. Res. *41*, 222–230.

54. Ortega, F., Gascón, S., Masserdotti, G., Deshpande, A., Simon, C., Fischer, J., Dimou, L., Chichung Lie, D., Schroeder, T., and Berninger, B. (2013). Oligodendrogliogenic and neurogenic adult subependymal zone neural stem cells constitute distinct lineages and exhibit differential responsiveness to Wnt signalling. Nat. Cell Biol. *15*, 602–613.

55. Azim, K., Rivera, A., Raineteau, O., and Butt, A.M. (2014). GSK3β regulates oligodendrogenesis in the dorsal microdomain of the subventricular zone via Wnt-β-catenin signaling. Glia *62*, 778–789.

56. Draganova, K., Zemke, M., Zurkirchen, L., Valenta, T., Cantù, C., Okoniewski, M., Schmid, M.-T., Hoffmans, R., Götz, M., Basler, K., and Sommer, L. (2015). Wnt/β-Catenin Signaling Regulates Sequential Fate Decisions of Murine Cortical Precursor Cells. Stem Cell. *33*, 170–182.

57. Gunhaga, L., Marklund, M., Sjödal, M., Hsieh, J.-C., Jessell, T.M., and Edlund, T. (2003). Specification of dorsal telencephalic character by sequential Wnt and FGF signaling. Nat. Neurosci. *6*, 701–707.

58. Chavali, M., Klingener, M., Kokkosis, A.G., Garkun, Y., Felong, S., Maffei, A., and Aguirre, A. (2018). Non-canonical Wnt signaling regulates neural stem cell quiescence during homeostasis and after demyelination. Nat. Commun. *9*, 36.

59. Obernier, K., Cebrian-Silla, A., Thomson, M., Parraguez, J.I., Anderson, R., Guinto, C., Rodas Rodriguez, J., Garcia-Verdugo, J.-M., and Alvarez-Buylla, A. (2018). Adult Neurogenesis Is Sustained by Symmetric Self-Renewal and Differentiation. Cell Stem Cell *22*, 221–234.e8.

60. Harris, L., Rigo, P., Stiehl, T., Gaber, Z.B., Austin, S.H.L., Masdeu, M.D.M., Edwards, A., Urbán, N., Marciniak-Czochra, A., and Guillemot, F. (2021). Coordinated changes in cellular behavior ensure the lifelong maintenance of the hippocampal stem cell population. Cell Stem Cell *28*, 863–876.e6.

61. Urbán, N., van den Berg, D.L.C., Forget, A., Andersen, J., Demmers, J.A.A., Hunt, C., Ayrault, O., and Guillemot, F. (2016). Return to quiescence of mouse neural stem cells by degradation of a proactivation protein. Science *353*, 292–295.

62. Liao, Y., Smyth, G.K., and Shi, W. (2013). The Subread aligner: fast, accurate and scalable read mapping by seed-and-vote. Nucleic Acids Res. *41*, e10.

63. Martin, M. (2011). Cutadapt removes adapter sequences from high-throughput sequencing reads. EMBnet. j. *17*, 10.

64. Liao, Y., Smyth, G.K., and Shi, W. (2014). featureCounts: an efficient general purpose program for assigning sequence reads to genomic features. Bioinformatics *30*, 923–930.

65. Love, M.I., Huber, W., and Anders, S. (2014). Moderated estimation of fold change and dispersion for RNA-seq data with DESeq2. Genome Biol. *15*, 550.

66. Madisen, L., Zwingman, T.A., Sunkin, S.M., Oh, S.W., Zariwala, H.A., Gu, H., Ng, L.L., Palmiter, R.D., Hawrylycz, M.J., Jones, A.R., et al. (2010). A robust and high-throughput Cre reporting and characterization system for the whole mouse brain. Nat. Neurosci. *13*, 133–140.

67. Scafidi, J., Hammond, T.R., Scafidi, S., Ritter, J., Jablonska, B., Roncal, M., Szigeti-Buck, K., Coman, D., Huang, Y., McCarter, R.J., et al. (2014). Intranasal epidermal growth factor treatment rescues neonatal brain injury. Nature *506*, 230–234.

STAR★METHODS

KEY RESOURCES TABLE

REAGENT or RESOURCE	SOURCE	IDENTIFIER
Antibodies		
Chicken anti βGal (1:2000)	Abcam	Cat#AB9361; RRID:AB_307210
Mouse anti APC (IgG2B; 1:100)	Calbiochem	Cat#OP80;
Mouse anti BrdU (G3G4; 1:1000)	DSHB	Cat#AB2314035
Rat anti Brdu (1:500)	abcam	Cat#AB6326; RRID:AB_305426
Rabbit anti Caspase-3 (1:1000)	Millipore	Cat#ABC495
Rat anti Ctip2 (1:500)	Abcam	Cat#AB18465; RRID:AB_2064130
Chicken anti GFP (1:1000)	AVES	Cat#NC9510598
Rabbit anti Cux1 (1:200)	Santa Cruz	discontinued
Rabbit anti Cux1 (1:300)	Proteintech	Cat#117331AP
Rabbit anti Mettl14 (1:1000)	Novus	Cat#NBP181392; RRID:AB_11021780
Rabbit anti Ki67 (1:500)	Thermo Scientific	Cat#RM910609
Rabbit anti MBP (1:1000)	Abcam	Cat#AB218011; RRID:AB_2895537
Goat anti Mcm2 (1:300)	Santa Cruz	Cat#SC9839; RRID:AB_648841
Goat anti Mcm2 (1:300)	R&D system	Cat#AF5778; RRID:AB_2141963
Mouse anti NeuN (1:1000)	Millipore	Cat#MAB377; RRID:AB_2298772
Guinea Pig anti NeuN (1:2000)	Synaptic system	Cat#266004; RRID:AB_2619988
Mouse anti Olig1 (IgG1; 1:500)	Neuromab	Cat#AB10674111
Rabbit anti S100β (1:5000)	Swant	discontinued
Guinea Pig anti S100β (1:2000)	Synaptic system	Cat#287004; RRID:AB_2620025
Mouse anti Olig2 (1:1500)	Millipore	Cat#MABN50; RRID:AB_10807410
Rabbit anti Olig2 (1:400)	Millipore	Cat#AB9610; RRID:AB_570666
Mouse anti Sox2 (1:100)	Sant Cruz	Cat#SC365823
Goat anti Sox2 (1:1000)	R&D system	Cat#AF2018; RRID:AB_355110
Rabbit anti Tbr2 (1:1500)	Abcam	Cat#AB2283; RRID:AB_302943
Rat anti Tbr2 (1:1000)	Invitrogen	Cat#14487582
Rabbit anti GSTpi (1:1000)	Enzo	Cat#ADIMSA102E
Goat anti Dcx (1:500)	Sant Cruz	Cat#SC8066
Donkey anti chicken FITC	Jackson Immunoresearch	Cat#703-095-155; RRID:AB_2340356
Donkey anti chicken biot	Jackson Immunoresearch	Cat#703-065-147
Donkey anti mouse 488	Thermo Fisher Scientific	Cat#A32766; RRID:AB_2762823
Donkey anti mouse 555	Thermo Fisher Scientific	Cat#A32773; RRID:AB_2762848
Donkey anti mouse 647	Thermo Fisher Scientific	Cat#31571; RRID:AB_162542
Goat anti mouse IgG1 555	Thermo Fisher Scientific	Cat#A21147; RRID:AB_2535783
Goat anti mouse IgG2b 555	Thermo Fisher Scientific	Cat # A-21147; RRID:AB_2535783
Goat anti mouse IgG1 647	Thermo Fisher Scientific	Cat # A-21240; RRID:AB_2535809
Goat anti mouse IgG2b 647	Thermo Fisher Scientific	Cat # A-21242; RRID:AB_2535811
Donkey anti mouse biot	Jackson Immunoresearch	Cat#715-065-150; RRID:AB_2307438
Donkey anti rat 488	Thermo Fisher Scientific	Cat#A-21208; RRID:AB_2535794
Donkey anti rat cy3	Jackson Immunoresearch	Cat#712-165-153; RRID:AB_2340667
Donkey anti rat 647	Jackson Immunoresearch	Cat#712-605-150; RRID:AB_2340693
Donkey anti rat biot	Jackson Immunoresearch	Cat#712-065-150; RRID:AB_2340646
Donkey anti rabbit 488	Jackson Immunoresearch	Cat#711-545-152; RRID:AB_2313584
Donkey anti rabbit 555	Thermo Fisher Scientific	Cat#A32794

(*Continued on next page*)

Continued

REAGENT or RESOURCE	SOURCE	IDENTIFIER
Donkey anti rabbit 647	Thermo Fisher Scientific	Cat#A31573
Donkey anti rabbit biot	Jackson Immunoresearch	Cat#711-065-152; RRID:AB_2340593
Donkey anti goat 488	Thermo Fisher Scientific	Cat#A-11055; RRID:AB_2762834
Donkey anti goat 555	Thermo Fisher Scientific	Cat#A-21432; RRID:AB_2535853
Donkey anti goat 647	Thermo Fisher Scientific	Cat#A-21447; RRID:AB_2535864
Donkey anti goat biot	Jackson Immunoresearch	Cat#705-065-147; RRID:AB_2340397
Donkey anti guinea pig 488	Jackson Immunoresearch	Cat#706-545-148; RRID:AB_2340472
Donkey anti guinea pig cy3	Jackson Immunoresearch	Cat#706-165-148; RRID:AB_2340460
Donkey anti guinea pig cy5	Jackson Immunoresearch	Cat#706-175-148; RRID:AB_2340462
Donkey anti guinea pig biot	Jackson Immunoresearch	Cat#706-065-148; RRID:AB_2340451
Alexa Fluor 405 conjugated streptavidin	Thermo Fisher Scientific	Cat#S32531
Fluorescien (DTAF) conjugated streptavidin	Jackson Immunoresearch	Cat#016-010-084; RRID:AB_2337236
Alexa Fluor 647 conjugated streptavidin	Jackson Immunoresearch	Cat#016-010-084
Chemicals, peptides, and recombinant proteins		
5-Bromo-2′-deoxyuridine (BrdU)	Sigma-Aldrich	Cat#B5002
5-Ethynyl-2′-deoxyuridine (EdU)	Sigma-Aldrich	Cat#900584
Tamoxifen	Sigma-Aldrich	Cat#T5648
Progesterone	Sigma-Aldrich	Cat#P8783
Type IV Hyaluronidase	Merck	H4272
Bovine Serum Albumin	Sigma-Aldrich	XXA9418
TopBlock	Lubio Science	SB232010
CHIR99021	Sigma aldrich	Cat#SML1046
DAPI	ThermoFisher Scientific	Cat#D1306
paraformaldehyde	Sigma aldrich	Cat#P6148
Critical commercial assays		
Click-iT® EdU Alexa Fluor 647 Imaging Kit	ThermoFisher Scientific	Cat#C10340
Deposited data		
BulkRNA-sequencing	This study	GSE233156
Experimental models: Organisms/strains		
Mouse: OF1	Charles River	MGI: 5649743
Mouse: Rosa YFP	The Jackson Lab	NA
Mouse: Neurog2CreERT2	Kind gift of F Guillemot	NA
Mouse: RosatdTomato	The Jackson Lab	RRID:IMSR_JAX:007914
Mouse: BAT-gal	The Jackson Lab	RRID:IMSR_JAX:005317
Recombinant DNA		
Plasmid: pCAG-Cre	Addgene	#13775
Plasmid: pCAG-EmGFP	VectorBuilder Inc., Cyagen Bioscience, Santa Clara, CA, USA	VB161220-1119syh
Plasmid: pCMV-hyPBase	Gift of L.López-Mascaraque, Instituto Cajal, Madrid, Spain	NA
Plasmid: pCAG-Mettl14	VectorBuilder Inc., Cyagen Bioscience, Santa Clara, CA, USA	VB1801111-1073pua
Software and algorithms		
Subread R package	Lia et al., 2013[62]	https://subread.sourceforge.net/
Cutadapt	Martin et al., 2011[63]	https://cutadapt.readthedocs.io/en/v4.5/index.html
featureCounts option	Liao et al., 2014[64]	https://subread.sourceforge.net/

(*Continued on next page*)

Continued

REAGENT or RESOURCE	SOURCE	IDENTIFIER
Dseq2 R package	Love et al., 2014[65]	https://bioconductor.org/packages/devel/bioc/vignettes/DESeq2/inst/doc/DESeq2.html
GraphPad PRISM 8	GraphPad Software	SCR_002798
Las AF	Leica	
ImageJ 1.51v	NIH	SCR_003070
Neurolucida 360	MBF Bioscience	SCR_016788
Zen 3.1 blue edition	Zeiss	
Photoshop CS4	Adobe	
Other		
Vibrating blade microtome	Leica	VT1000 S
TCS SPE confocal microscope	Leica	SCR_002140
TCS SP5 confocal microscope	Leica	SCR_018714
DM5500 epifluorescent microscope	Leica	
Zeiss Axio Scan.Z1	Zeiss	SIP 57154
Electroporator NEPA21 type II	Nepa Gene	
Tweezers Electrode	Nepa Gene	CUY650
Signa gel	Parker Laboratories	15–20
Animal chamber	Biospherix	A15274P
Oxygen chamber controller	Biospherix	P110RS485
Cell sorter	Becton Dickinson	BD® FACSAria II
Sequencer	Illumina	NextSeq 500

RESOURCE AVAILABILITY

Lead contact

Further information and requests for resources and reagents should be directed to and will be fulfilled by the lead contacts, Olivier Raineteau (olivier.raineteau@inserm.fr).

Materials availability

Unique resources and reagents generated in this study are available from the lead contact with a completed Material Transfer Agreement.

Data and code availability

- Bulk RNA-sequencing data have been deposited at GEO (GSE233156) and are publicly available as for the date of publication. Accession numbers are listed in the key resources table. Microcopy data reported in this paper will be shared by the lead contact upon request.
- This paper does not report original code.
- Any additional information required to reanalyze the data reported in this paper is available from the lead contact upon request.

EXPERIMENTAL MODEL AND STUDY PARTICIPANT DETAILS

Animals

Experiments were conducted on embryonic, neonatal and young adult (E13 and E15; P3, P5, P11, P13, P15 and P19; P45 and P90, respectively) male and female. For all experiments (fate mapping and glutamatergic progenitors labeling), the morning when the plug was observed was considered as E0.5 and the day of birth was defined as postnatal day (P)0. Mice of several strains were used: wilt-type OF1 mice (Charles River, France); Rosa-YFP mice (ROSA26-Flox-Stop-Flox YFP, Jackson Laboratories); Neurog2CreERT2/tdTom[66] and BAT-gal.[26] Mice were housed in plastic cages (group-housed) with food and water *ad libitum* and kept in 12:12h light/dark cycles (room temperature = 22 ± 1°C). All procedures were performed in accordance with European requirements 2010/63/UE and have been approved by the Animal Care and Use Committee CELYNE (APAFIS#187 & 188). Animal procedures were executed in accordance with French law, with strict consideration given to the care and use of animals. Mice were randomly assigned to experimental groups.

METHOD DETAILS

In-vivo

Tamoxifen administration

Tamoxifen (Sigma-Aldrich) and progesterone (Sigma-Aldrich) were dissolved in Corn oil (Sigma-Aldrich, C8267) at final concentration of 20 mg/mL and 10 mg/mL, respectively. Pregnant Neurog2CreERT2/tdTom females were administered 0.5 mg tamoxifen and 0.25 mg progesterone by gavage at E13.5 or E15.5 and terminated 12h later. Mouse pups were injected subcutaneously with 1 mg tamoxifen at P12 and were terminated 18h later.

Electroporation

Postnatal electroporation was performed on mice at P1, as previously described.[32] For permanent labeling of NSCs, a pCAGs-Cre plasmid under a chicken β-actin promoter (pCAG-Cre plasmid; plasmid #13775, Addgene) was used to allow the permanent expression of Yellow Fluorescent Protein (YFP) in NSCs and their progeny coming from V-SVZ in Rosa-YFP mice. Alternatively, a pPB(Exp)-CAGG>3xNLS/EmGFP plasmid (pPB-EmGFP plasmid; plasmid #VB161220-1119syh, VectorBuilder) with the insertion of Emerald GFP (EmGFP) and the co-electroporation of a transposon containing plasmid pRP[Exp]-Puro-CAGG>Pbase (pCMV-hy-PBase plasmid; Gift of L.López-Mascaraque) allowing the nuclear integration in OF1 mice were used. Mettl14 GoF experiments were performed with prP[Exp]-EGFP6Cag>mMetll14[NM_201638.2]* plasmid (pCAG-Mettl14 plasmid; #VB1801111-1073pua, VectorBuilder) was used within both OF1 for fate mapping and in BAT-gal transgenic mice for measurement of Wnt/β-catenin pathway activity following Mettl14 GoF. The following electroporation parameters were used: 5 pulses at 95 V of 50 ms separated by 950 ms using an Electroporator NEPA21 type II (Nepa Gene) and tweezer electrodes (Nepa Gene) coated with a conductive gel Signa gel (Parker Laboratories).

Hypoxia

Mice aged P3 placed in a hypoxic rearing chamber (Biospherix) maintaining at 10 ± 0.5% O2 concentration by displacement with N2 as described previously.[17,21] Hypoxia began at P3, for 8 days, until P11. A separate group was maintained in a normal atmosphere (normoxic group; Nx). Foster mothers were used to conserve milk quality under a hypoxic environment, control mother and hypoxic mother were exchanged at P6 and P9.

BrdU/EdU administrations

Labeling of quiescent NSCs (qNSCs) was performed using a single injection of bromodeoxyuridine (BrdU; Sigma-Aldrich) (or deoxyuridine; EdU; Sigma-Aldrich) at E14, time were the maximum of NSCs enter into quiescence.[29] Labeling and fate mapping of cycling cells was performed using single or repeated BrdU (or EdU) injections at E13 and E15 and between P3 to P11 as well as between P11 to P12. BrdU or EdU was dissolved in Dulbecco's Phosphate Buffered Saline (DPBS; Sigma-Aldrich) at 10 mg/mL and was shaken until it was completely dissolved. For intraperitoneal injections (IP) 50 mg/kg was administered.

Labeling of transiently active NSCs (taNSCs) was performed using a chronic BrdU administration in drinking water during postnatal period between P45 to P59 [27]. BrdU was dissolved in water with 10 mg/mL of sucrose in a concentration of 1 mg/mL, and changed every two days.

Intranasal drug administration

The Gsk3b inhibitor CHIR99021 (Sigma-Aldrich) was administered by intranasal administration as previously described.[21,67] Mucus was first permeabilized by the use of type IV hyaluronidase, then, 10 μL of CHIR99021 (Sigma-Aldrich) was administered 4 times (starting at the end of the hypoxic period, then every 12 h), at a concentration of 1.5 mM in sterile DPBS (Sigma-Aldrich).

Ex-vivo

Immunohistochemistry

Mice were sacrificed by an intraperitoneal overdose of pentobarbital followed by perfusion with Ringer's Lactate solution and 4% paraformaldehyde (PFA; Sigma-Aldrich) dissolved in 0.1 M phosphate buffer (PB; pH 7.4). Brains were removed and post fixed for 12–48 h at 4°C in 4% PFA and sectioned in 50-μm thick coronal serial sections by using a vibratome VT1000 S (Leica). When necessary, antigen retrieval was performed for 20 min in citrate buffer (pH 6; Sigma-Aldrich, 21545) at 80°C, then cooled for 20 min at room temperature and washed in 0.1 M PB. Blocking was performed in a TNB buffer (0.1 M PB; 0.05% Casein (Sigma-Aldrich, C5890); 0.25% Bovine Serum Albumin (Sigma-Aldrich, A9418); 0.25% TopBlock (Lubio Science, SB232010)) with 0.4% Triton X-(Sigma-Aldrich, T9284; TNB-Tx) for 2 h at room temperature. Sections were then incubated overnight at 4°C with gentle shaking in TNB-Tx solution and with primary antibodies (see key resources table). Following extensive washing in 0.1 M PB with 0.4% Triton X-(PB-Tx), sections were incubated in TNB-Tx solution with appropriate secondary antibodies conjugated Alexa Fluor for 2 h at room temperature. Sections were washed and counterstained with DAPI (ThermoFisher Scientific, C10646).

To amplify the signal and to perform 405 stainings, biotinylated secondary antibodies were used in combination with DTAF conjugated streptavidin or Alexa 405/555/647 conjugated streptavidin.

Revelation of EdU was done using Click-itTM, EdU cell proliferation Kit for imaging, Alexa fluorTM 555 or 647 dye (Thermo Fisher scientific).

For BrdU revelation a step of acidic incubation was used (HCl 2N; Sigma-Aldrich, 258148) for 20 min at 37° followed by a Borate 0.1M (Fisher scientific, 15415199) incubation during 30 min.

Cell capture

cDNA library preparation and sequencing: The brains of E14, E16, P13 (control and hypoxic) were harvested and placed on ice-cold Hank's balanced salt solution (HBSS, ThermoFisher Scientific, 11530476) for microdissection. The region of intense tdTomato expression (i.e., dorsal pallium) were then microdissected and cells were finally chemically (Trypsin-EDA 0.05%; Life Technologies, 15090046) and manually (1000 μL pipet) dissociated. The cell suspension was FAC-sorted on a BD FACSAria to isolate tdTom+ cells, DAPI (ThermoFisher Scientific) was used to select only viable cells. For each condition, tissue collection, Fluorescence-Activated Cell Sorting (FACS) and cell isolation were performed in two independent replicates and in three for postnatal controls to ensure biological significance. A minimum of 30.000 cells was used for each replication. The RNA sequencing was performed by Bulk technology.

RNA sequencing and differential gene expression analysis

Purified mRNAs (400 pg) from each sample were amplified and libraries prepared from 1ng of amplified cDNA using NEBNext Ultra II RNA Library Prep Kit for Illumina (New England BioLabs, E7770S). Single-end sequencing reads (75bp) were generated using NextSeq 500 sequencer (Illumina) with at least 120 million reads for each sample. Quality of sequenced reads were assessed using FastQC (https://www.bioinformatics.babraham.ac.uk/projects/fastqc/). PolyA/T tails were trimmed using Cutadapt.[63] The trimmed reads were aligned to the reference mouse genome (GRCm38) using Subread R package.[62] Fragment numbers were counted using the featureCounts option.[64] Normalization and extraction of differentially expressed genes (DEGs) between conditions were performed using the DESeq2 R package.[65]

Microscopy

Images were acquired using a Zeiss Axio Scan.Z1 (Zeiss Microsystems), Leica DM5500 epifluorescent microscope, Leica TCs SPE II and a TCs Leica SP5 confocal laser microscopes (Leica Microsystems), using 10x/0.3 NA dry objective (HCX PL Fluotar); 20×/0.70 NA dry objective (HC PL APO CS); 20×/0.70 NA oil objective (HX PL APO CORR CS); 40×/1.25 NA oil objectives (HCPL Fluotar) and software's Zen (Zen 3.1, Blue edition) and LAS (Leica Microsystems, V3.1.2.16221).

QUANTIFICATION AND STATISTICAL ANALYSIS

Quantifications were performed on coronal sections by counting the number of cells from z stack of confocal images on ImageJ v1.51 software (national institute of health, USA). Cell counts were performed using z-stacks of confocal images, which granted accurate visualization of the cells. The N values represent the number of mice and the n values represent the number of cells, this information was added to figure legends. Animals were randomly assigned to groups. All data are shown as mean ± SEM; as median and quartile and statistical significance was calculated using GraphPad PRISM 8 and using appropriate tests (unpaired/paired t-test and one- or two-way ANOVA followed by Bonferroni post-hoc test), this information appears within the figure's legend. For statistical comparisons, differences were considered statistically significant when the p-values were <0.05. Statistical significance was defined at $*p < 0.05$; $**p < 0.01$; $***p < 0.001$. For every experiment, statistical tests and significance and n values are indicated in figure legends. Images were assembled as representative pictures using Las-X and photoshop (CS4). Quantification procedures and statistical tests used for every analysis are indicated in detail below.

Animal and brain weights

To determine the impact of hypoxia on animals and brain development. Mice were weighted at the end of the hypoxic period (P11). Ten mice were weighted in each group. Brain were weighted after intracardiac perfusion and brain extraction at the end of the hypoxic period (P11). Six normoxic and eight hypoxic brains were weighted. Data are expressed as mean weight (g) ± SEM. Statistical analysis were performed through parametric unpaired t-test (Figures S1B and S1C).

Cortical volume

To determine the extent of cortical volume loss following hypoxia. We measured the thickness of the cortex on a homogeneous series of coronal sections and extrapolated the volume (μm^3) from these results. Thirteen normoxic and fourteen hypoxic cortical volume were quantified. Data are expressed as mean volume (μm^3) ± SEM. Statistical analysis was performed through parametric unpaired t-test (Figure S1D).

Dorsal V-SVZ area

To determine the impact of hypoxia on cortical germinal region. We measured the area (μm^2) of the dorsal V-SVZ within the rotrocaudal axis on three coronal sections in each animal. Five normoxic and five hypoxic animals were quantified. Data are expressed as mean area (μm^2) ± SEM. Statistical analysis was performed through parametric unpaired t-test (Figures S1K and S1L).

Quantification of cell fate

To determine cell fate following hypoxia and/or manipulation on V-SVZ NSCs activity and fate. Positive cells for marker(s) of interest(s) was(ere) quantified through z-stacks. Depending on the analysis, quantifications were done either on an entire series of sections or on at least 3 equally spaced sections of the V-SVZ or cortical area or olfactory bulbs.

RESULTS PRESENTED AS RAW NUMBER OF CELLS *PER* SECTION

Quantifications for apoptosis (cas3+) were performed within the cortex at the end of the hypoxic period (P11). Seven normoxic and six hypoxic animals were quantified (Figure S1F). Quantifications for quiescent and transiently active NSC populations were performed in the dorsal, lateral and ventral V-SVZ domains. Quiescent NSCs were quantified at P11, P19, P45 (normoxic and hypoxic + CHIR9901) and P90, transiently active at P90 following thymidine analog administration from P45 to P59 and a chasing period of 31 days. Quantifications of active and proliferative NSCs were performed at dorso-lateral and ventral corners of the V-SVZ at P45. Five mice were quantified for qNSCs in each group, four mice were quantified for taNSCs in each group, four normoxic mice and three hypoxic+CHIR9901 mice for aNSCs and pNSCs (Figures 5D–5G and S5A). Data are expressed as mean number of positive cells per sections ± SEM. Statistical analysis were performed through parametric unpaired t-test.

RESULTS PRESENTED AS NUMBER OF CELLS *PER* VOLUME

Quantifications of fate mapped embryonic (E13 and E15) NSCs differentiating into cortical neurons (Edu+BrdU + Cux1+/Ctip2+) were performed within the cortex of hypoxic mice at P19. We counted the number of positive cells on coronal sections and extrapolated numbers to volume (mm^3). Four mice were quantified in each group (Figures 2I and 2J). Data are expressed as mean volume (mm^3) ± SEM. Statistical analysis was performed through parametric unpaired t-test.

RESULTS PRESENTED AS PERCENTAGES OF CELL ON A CELLULAR POPULATION

Quantifications for oligodendrocytes maturation blockade following hypoxia (Olig2+CC1+/Olig2+) were performed within the cortex at the end of the hypoxic period (P11). Five mice were quantified in each group (Figure S1H).

Quantifications of cycling GLU and oligodendroglial progenitors (%Tbr2+Ki67+/Tbr2+; %Olig2+Ki67+/Olig2+) were performed in the dorsal V-SVZ at the end of the hypoxic period (P11). Eight mice were quantified in each group (Figures 1D and 1E).

Quantifications of GFP+ RG like cells (GFP+RG like/GFP+ cells) were performed in dorsal V-SVZ at the end of the hypoxic period (P11) by plotting GFP+ cells that present an RG morphology among the total number of GFP+ cells. Three normoxic and four hypoxic mice were quantified (Figure 1I).

Quantification of cycling GFP+ cells following Mettl14 GoF (% GFP+Ki67+/GFP+) were performed within the dorsal V-SVZ at P5 (4-day post-electroporation). Four controls and five Mettl14 OE mice were quantified (Figure 3I).

Quantifications of βGal activity following hypoxia and CHIR9901 treatment in GLU and glial progenitors (%Tbr2+βGal+/Tbr2+; %Olig2+ βGal+/Olig2+) were performed in dorsal V-SVZ at P15. Four normoxic, three hypoxic and five hypoxic+CHIR9901 mice for GLU progenitors and three normoxic, three hypoxic and five hypoxic+CHIR9901 mice for oligodendroglial progenitors were quantified (Figures 4H and 4I).

Quantifications of qNSCs and taNSCs were performed at P45 (qNSCs) or P90 (taNSCs) within the dorsal, lateral and ventral microdomains of the V-SVZ. Five mice for qNSCs in each group and four mice for taNSCs in each group were quantified (Figures S5 C, S5E and S5G).

For all quantifications, data are expressed as mean percentages ± SEM. Statistical analysis were performed through parametric unpaired t-test and one-, two-way ANOVA followed by Bonferroni post-hoc.

RESULTS PRESENTED AS PERCENTAGES OF CELL COMPARED TO CONTROL

Quantifications for cycling cells (%Ki67+ cells/controls) were performed in dorsal V-SVZ at the end of the hypoxic period (P11). Eight mice were quantified in each group (Figure 1C).

Quantifications of GLU and glial progenitors' populations (%Tbr2+ & Olig2+ cells/controls) were performed in dorsal V-SVZ before (P3), at the end (P11) and following (P15 & P19) hypoxic period. Three mice were quantified at P3, P15, P19 and eight mice a P11 (Figure 1F).

Quantifications of maintenance of radial glial cells (%GFP+ radial processes/controls) were performed at the end of the hypoxic period (P11) or at P5 (4day post electroporation) by drawing a line immediately above the corpus callosum to count the number of GFP+ processes intersecting with it. Results were normalized by the total number of GFP+ cells within the dorsal V-SVZ. Four normoxic mice and five hypoxic mice (Figure 1I); five control and Mettl14 GoF mice (Figure 3G) were quantified.

Quantification of BrdU+ neurons (%BrdU+NeuN+/Controls) within the olfactory bulbs were performed at P90 following chronic administration of BrdU in the drinking water from P45 to P59. Four mice were quantified in each group (Figure 5H).

Quantification of neuroblasts in olfactory bulbs (%Dcx+/control) were performed at P90. Four mice were quantified in each group (Figure 5I).

Quantification of pNSCs in the dorso-lateral corner of the V-SVZ were performed at P45 and P90. Four normoxic and three hypoxic+CHIR9901 P45 and four P90 mice in each group were quantified (Figure S5I).

Data are expressed as mean percentage ± SEM. Statistical analysis were performed through parametric unpaired or paired t-test or two-way ANOVA followed by Bonferroni post-hoc.

RESULTS PRESENTED AS PERCENTAGE OF CELLS

Quantifications for neuronal versus glial fate mapping (%YFP+ cortical cells neuronal vs. glial) were performed within the cortex at P19 by plotting GFP+ cells based on their morphology. Four normoxic and eight hypoxic mice were quantified (Figure S2D).

Quantifications for neuronal distribution (GFP+Cux1±Ctip2±; % neurons) were performed in hypoxic mice within the cortex at P19 by plotting the number of GFP+ neurons expressing either Cux1 or Ctip2 in function to their localization (upper/deeper layers). Nine mice were quantified in each group (Figure 1N).

Quantification of marker acquisition following hypoxia and treatment (CHIR9901) were performed within the cortex at P19 (P45 for GSTpi) by plotting the GFP+ cells (neurons or oligodendrocytes) based on their expression of Cux1 or Ctip2 or none (neurons) or based on their morphology or expression of CC1/Olig1 and CC1/GSTpi (Oligodendrocytes). For neuronal fate twelve hypoxic and six hypoxic+CHIR9901, for morphology glial fate five normoxic and hypoxic and four hypoxic+CHIR9901, for glial CC1/Olig1 outcome six normoxic and five hypoxic ± CHIR9901, for glial GSTpi/CC1 outcome four normoxic and three hypoxic ± CHIR9901 mice were quantified (Figures 4J and 4N–4P).

Data are expressed as mean percentage ± SEM. Statistical analysis were performed through parametric two-way ANOVA followed by Bonferroni post-hoc.

RESULTS PRESENTED AS OPTICAL DENSITY MEASUREMENTS

Quantifications of optical density (OD) for myelin protein (MBP) were performed at the end of the hypoxic period (P11) within the corpus callosum area that was delineated based on DAPI counterstaining. Five mice were quantified in each group (Figure S1J).

Quantifications of Mettl14 OD in Tbr2+ cells were performed based on Tbr2+ cells at P13. Five normoxic and four hypoxic mice were quantified. The OD of the Mettl14 signal was measured for 710 normoxic Tbr2+ cells and 570 hypoxic Tbr2+ cells (Figure 3D).

Quantifications of βGal OD were performed within the embryonic pallium (E13, E15) or postnatal dorsal V-SVZ (P1, following hypoxia (P11) and treatment (P15)) that were delineated based on DAPI counterstaining. Nine E13, three E15, six P1, six normoxic P11, ten hypoxic P11, seven normoxic P15, three hypoxic P15 and five hypoxic+CHIR9901 P15 mice were quantified (Figures 4B and 4G and S4B). βGal optical density was also quantified in GFP+ cells (control vs. Mettl14 GoF) based on GFP+ cells at P3 (two days post-electroporation). Four mice were quantified; 326 control cells and 381 Mettl14 GoF cells were measured for βGal (Figure 4E).

Data are expressed as mean OD ± SEM or with median and quartile. Statistical analyses were performed through parametric unpaired t-test and two-way ANOVA followed by Bonferroni post hoc.

Morphological analysis

To analyze morphological features of hypoxia induced neurons, Confocal images of GFP+ cortical neurons following electroporation and hypoxia ± CHIR9901 were taken with a z-step of 0.3μm and a xy resolution of 1024*1024. Three-dimensional analysis of dendritic arborization of GFP+ neurons following hypoxia ± CHIR9901 (GFP+Cux1±Ctip2±) were performed using Neurolucida 360 software (MBF Bioscience) at P19. We performed a Sholl analysis to determine the complexity of the dendritic arborization and a quantification of the number of nodes and the total length of the dendritic arborization (μm). Twenty-three GFP+Ctip2+ and seven GFP+Cux1+ neurons were reconstructed (Figures 4L and S2F–S2H). Data are expressed as mean percentage ± SEM. Statistical analysis were performed through two-way ANOVA followed by Bonferroni post-hoc and parametric unpaired t-test.

Differential gene expression

To determine transcripts enriched or repressed in GLU progenitors and conditions, bulk RNA-sequencing was performed. Differentially expressed genes (DEG) were identified based on Log2 fold change (Log2FC), as well as p- value or pAdjusted. To represent the rejuvenation observed following hypoxia (Figure 2C), we highlight (red dots) repressed and enriched transcripts following hypoxia based on Log2FC > 2 and p-value <10e-6. To highlight m6a and Wnt signaling enrichment in GLU progenitors flowing hypoxia we extracted m6a writers, readers and erasers (Figure 3C) as well as Wnt activators and inhibitors (Figure 4C). We then calculated their p-value between normoxic and hypoxic conditions.

Over representation analysis (ORA) & gene ontology (GO) analyses

We performed ORA analyses with DEG (Log2FC > 2, p-value<0.05) by interrogating DAVID data web interface (https://david.ncifcrf.gov/) for GO associated to biological processes (BP). To interrogate GO BP similarities between embryonic/postnatal and hypoxia we used the top 1000 transcripts (based on pAdjusted). We measured similarities between conditions based on the percentage of transcripts in GO terms (Figures 2D and S3B). To identify embryonic biological processes reactivated by hypoxia, we used transcripts enriched in both condition (350 transcripts, see Figure 2B). To identify biological processes specific to hypoxia, we used transcripts enriched following hypoxia while excluding transcripts associated to normal postnatal development (373 transcripts, see Figure 2B). Results were ranked on p-value<0.01 (Figure 3B) or % of genes within significantly enriched GO categories (Figures 2D, S3D and S3E).